

(2)

RDA-TR-0030-0001-001

AD-A225 999

MODELING THE DYNAMIC LOAD/UNLOAD BEHAVIOR
OF CERAMICS UNDER IMPACT LOADING (U)

By:
J.R. FURLONG
M.L. ALME
J.F. DAVIS

DTIC
ELECTE
AUG 29 1990
S D

JULY 1990

Final Report

In Support of
Contract No.: DAAL03-89-C-0019

Prepared for:
U.S. ARMY RESEARCH OFFICE
P.O. Box 12211
Research Triangle Park, NC 27709-2211

RDA
LOGICON

R & D ASSOCIATES

DISTRIBUTION STATEMENT A

Approved for public release
Distribution Unlimited

2100 WASHINGTON BLVD. • ARLINGTON, VA 22204-5706 • TELEPHONE: (703) 486-3500

UNCLASSIFIED

SECURITY CLASSIFICATION OF THIS PAGE

REPORT DOCUMENTATION PAGE

1a. REPORT SECURITY CLASSIFICATION Unclassified			1b. RESTRICTIVE MARKINGS		
2a. SECURITY CLASSIFICATION AUTHORITY			3. DISTRIBUTION/AVAILABILITY OF REPORT Approved for public release; distribution unlimited.		
2b. DECLASSIFICATION/DOWNGRADING SCHEDULE			4. PERFORMING ORGANIZATION REPORT NUMBER(S)		
5. MONITORING ORGANIZATION REPORT NUMBER(S) ARO 27116.1-MS-A			6a. NAME OF PERFORMING ORGANIZATION R & D Associates		
6b. OFFICE SYMBOL (If applicable)			7a. NAME OF MONITORING ORGANIZATION U. S. Army Research Office		
6c. ADDRESS (City, State, and ZIP Code) 301 South West Street Alexandria, VA 22314			7b. ADDRESS (City, State, and ZIP Code) P. O. Box 12211 Research Triangle Park, NC 27709-2211		
8a. NAME OF FUNDING/SPONSORING ORGANIZATION U. S. Army Research Office			8b. OFFICE SYMBOL (If applicable)		
9. PROCUREMENT INSTRUMENT IDENTIFICATION NUMBER DAAL03-89-C-0019			10. SOURCE OF FUNDING NUMBERS		
8c. ADDRESS (City, State, and ZIP Code) P. O. Box 12211 Research Triangle Park, NC 27709-2211			PROGRAM ELEMENT NO.	PROJECT NO.	TASK NO.
11. TITLE (Include Security Classification) Modeling the Dynamic Load/Unload Behavior of Ceramics under Impact Loading			12. PERSONAL AUTHOR(S) J. R. Furlong, J. F. Davis and M. L. Alme		
13a. TYPE OF REPORT FINAL		13b. TIME COVERED FROM 15Jul89 TO 14Jul90		14. DATE OF REPORT (Year, Month, Day) 90 July 31	
15. PAGE COUNT 56		16. SUPPLEMENTARY NOTATION The view, opinions and/or findings contained in this report are those of the author(s) and should not be construed as an official Department of the Army position, policy, or decision, unless so designated by other documentation.			
17. COSATI CODES		18. SUBJECT TERMS (Continue on reverse if necessary and identify by block number)			
FIELD	GROUP	SUB-GROUP	Armor Ceramics		
			Ballistics, Ceramics		
			Ceramics, modeling of		
			Ceramics, impact loading of		
19. ABSTRACT (Continue on reverse if necessary and identify by block number) The RDA ceramic failure model was used to model the behavior of SiC and B ₄ C during plate impact loading. The experiments modeled were performed at Sandia National Laboratory (Kipp and Grady, 1989). The simulations were performed with a version of the Sandia WONDY-V hydrocode (Kipp and Lawrence, 1981) that was modified to run on a PC and to include the RDA ceramic failure model. The model adequately characterizes the two ceramic materials although B ₄ C and SiC exhibit distinctly different degrees of work hardening, strain rate hardening, and damage sensitivity. Both materials experienced damage (micro-cracking) on load which was predicted by the model. The experimental unloading data exhibits a reduced magnitude elastic unload (cont.)					
20. DISTRIBUTION/AVAILABILITY OF ABSTRACT <input type="checkbox"/> UNCLASSIFIED/UNLIMITED <input type="checkbox"/> SAME AS RPT. <input type="checkbox"/> DTIC USERS			21. ABSTRACT SECURITY CLASSIFICATION Unclassified		
22a. NAME OF RESPONSIBLE INDIVIDUAL			22b. TELEPHONE (Include Area Code)		22c. OFFICE SYMBOL

19. ABSTRACT (cont.)

wave which suggests that further damage has accumulated after the ceramic reaches peak stress. A strength reducing mechanism such as fatigue, or melting at grain boundaries are suspected as the cause of this unpredicted strength loss.

No spall was evident in the measured signals and the model predicts spall will not occur. The predicted axial stress levels were significantly above the estimated spall strengths of the two ceramics. Failure was prevented by positive (compressive) mean stress levels that were maintained throughout the ceramic specimen during the experimental measurement. Therefore, a suggested conclusion is that for tensile failure to occur in these ceramics, the mean stress must be negative (tensile). JSI

MODELING THE DYNAMIC LOAD/UNLOAD BEHAVIOR
OF CERAMICS UNDER IMPACT LOADING

FINAL REPORT

J.R. Furlong, M.L. Alme, and J.F. Davis

August 1989 - 14 July 1990

U. S. ARMY RESEARCH OFFICE

CONTRACT DAAL03-89-C-0019

R & D ASSOCIATES

APPROVED FOR PUBLIC RELEASE;
DISTRIBUTION UNLIMITED

Accession For	
NTIS	CFA&I <input checked="" type="checkbox"/>
DTIC	TAB <input type="checkbox"/>
Unannounced <input type="checkbox"/>	
Justification	
By	
Distribution/	
Availability Codes	
Dist	Avail and/or Special
A-1	



TABLE OF CONTENTS

	PAGE
LIST OF FIGURES	ii
ABSTRACT	1
1. INTRODUCTION	2
2. REVIEW OF RDA CERAMIC FAILURE MODEL	3
3. MODELING METHODOLOGY	5
4. PC-WONDY COMPUTER CODE	10
5. SANDIA PLATE IMPACT EXPERIMENTS	11
6. MODEL RESULTS	12
6.1 Ceramic Properties	12
6.1. Model Results for SiC	12
6.2. Model Results for B ₄ C	16
7. SUMMARY	20
BIBLIOGRAPHY	22
APPENDIX 1. RDA/UDRI CERAMIC FAILURE MODEL	45
APPENDIX 2. FORMULARY	51

LIST OF ILLUSTRATIONS

FIGURE		PAGE
1.	Elastic perfectly-plastic stress-strain path showing relationship to the hydrostat (heavy line). Dashed line illustrates response with softening such as damage.	24
2.	Schematic of Hugoniot for a ceramic material with porosity indicating that at each initial specific volume, the material will have a different HEL and potentially different longitudinal modulus. Loss of strength due to damage in the material collapses the Hugoniot toward the hydrostat of the fully dense material.	25
3.	Idealized load/unload wave profiles for planar impact experiments.	26
4.	Plate impact experimental configuration of Sandia National Laboratory experiments (Kipp and Grady, 1989).	27
5.	Experimental results for SiC for plate impact velocities as indicated using the experimental configuration of Figure 4 (Kipp and Grady, 1989).	28
6.	Experimental results for B ₄ C for plate impact velocities as indicated using the experimental configuration of Figure 4 (Kipp and Grady, 1989). Note the dispersive unload behavior and absence of apparent strength on unload.	29
7.	Least squares fit to Hugoniot data for SiC (LANL, 1980) using equation 5 for η values greater than 0.15 (solid line). The dashed line represent elastic perfectly-plastic behavior.	30
8.	Least squares fit to experimental Hugoniot data for B ₄ C (Gust et al, 1971) using equation 5 for η values greater than 0.15 (solid line). The dashed lines represent elastic perfectly-plastic behavior.	30
9.	Comparison of PC-WONDY model predictions and experimental data (Kipp and Grady, 1989) for SiC using an elastic perfectly-plastic model; (a) for plate impact velocity of 2100 m/s and (b) for plate impact velocity of 1542 m/s. This model shows clearly an absence of accurate yield function, the reflection of the LiF window and the presence of an anomalous wave at approximately 1.7 μ s.	31

10. Model predictions for 2100 m/s plate impact experiments with SiC with an increase in the strain rate hardening term, increases the apparent HEL, increases the magnitude of the elastic unload and causes the unload wave to arrive earlier. (a) Perfectly-plastic, (b) $C_3 = 0.01$, (c) $C_3 = 0.02$, and (d) $C_3 = 0.03$. 32
11. A systematic variation of initial yield, strain hardening parameters, strain rate hardening and damage coefficients for SiC yields a good fit for the load and elastic unload for planar impact experiments (Kipp and Grady, 1989) for impact velocity of 2100 m/s. (a) $C_1 = 80$ kbar, (b) $C_1 = 80$ kbar, $C_2 = 100$ kbar, and $n = 0.1$, (c) $C_1 = 80$, $C_2 = 100$, $n = 0.1$, $\alpha = 0.7 \times 10^{-6}$ kg/J, and (d) $C_1 = 80$, $C_2 = 100$, $n = 0.1$, $\alpha = 0.7 \times 10^{-6}$ kg/J and $C_3 = 0.008$. 33
12. Comparison of PC-WONDY model predictions with experimental results for SiC with plate impact velocity of 2100 m/s using the parameters $C_1 = 80$, $C_2 = 100$, $n = 0.1$, $\alpha = 0.7 \times 10^{-6}$ kg/J, and $C_3 = 0.008$ with the unload isentrope having 30 kbar offset at zero strain. As shown, these results compare favorably with the experimental data (Kipp and Grady, 1989). 34
13. Comparison of PC-WONDY model predictions with experimental results for SiC with plate impact velocity of 1540 m/s using the parameters $C_1 = 80$, $C_2 = 100$, $n = 0.1$, $\alpha = 0.7 \times 10^{-6}$ kg/J, and $C_3 = 0.008$ with the unload isentrope having 30 kbar offset at zero strain. As shown, these results compare favorably with the experimental data (Kipp and Grady, 1989) for 1.2 μ s after plate impact (loading waves), but does not model the unload adequately. 35
14. Hypothetical velocity history showing the abrupt slope change that is associated with spall. 36
15. Calculated pressure distribution versus position for SiC with a plate impact velocity of 2100 m/s when the pressure reaches its absolute minimum in the target plate. 37
16. Calculated pressure distribution for SiC with a plate impact velocity of 2100 m/s when the lithium fluoride window has been removed. Note the signature of a spall zone at a position 6 to 7 mm from the flyer/target plate interface. 37

17. Model predictions with an increase in the damage coefficient α using the parameters; $C_1 = 80$, $C_2 = 100$, $n = 0.1$, and $C_3 = 0.008$ for SiC with plate impact velocity of 2100 m/s reduces the elastic unload and shows a more dispersive plastic unload wave. (a) $\alpha = 0.6 \times 10^{-6}$, (b) $\alpha = 2 \times 10^{-6}$, (c) $\alpha = 3 \times 10^{-6}$, and (d) $\alpha = 4 \times 10^{-6}$. 38
18. Comparison of PC-WONDY model predictions with experimental data for SiC with plate impact velocity of 1540 m/s and with increased damage accumulation. The damage was increased from 6 - 8 percent (see figure 15) to 40 percent. This produces good agreement to the experimental data shown with the heavy line (Kipp and Grady, 1989), for times greater than 1.3 μ s after plate impact. Suggestion is that after the loading phase, damage continues to accumulate, reaching a level of about 40 percent by the time unloading begins. 39
19. Least squares fit of Hugoniot data for B_4C (Gust et al, 1971) using equation (7) for values of η greater than 0.15 (solid line). The observed $\Delta\eta$ at constant stress for $\eta = .055$ to .065 is indicative of possible loss of porosity or phase change in the ceramic. The shape of the underlying hydrostat is therefore not known. 40
20. Comparison of PC-WONDY model predictions with experimental data for B_4C using an elastic perfectly-plastic model for plate impact velocity of 1550 m/s. Experimental results shown with the heavy line (Kipp and Grady, 1989). 41
21. Model predictions of velocity history curves for B_4C for plate impact velocity of 1550 m/s with variation in the damage sensitivity. Increases in α delays the arrival time of the plastic shock. The elastic unloading wave begins to catch up to the plastic load, overtaking it in (d). (a) Perfectly-plastic, (b) $\alpha = 1.0 \times 10^{-5}$, (c) $\alpha = 2.0 \times 10^{-5}$, and (d) $\alpha = 3.0 \times 10^{-5}$. 42
22. Comparison between model predictions and measured velocity histories for B_4C , using $\alpha = 3.4 \times (10)^{-5}$ kg/J, $C_1 = 116$, and no work hardening or strain rate hardening adequately fits the loading waves for plate impact velocity of 1550 m/s. Heavier curve is experimental data (Kipp and Grady, 1989). 43
23. Comparison between model predictions and measured velocity histories for B_4C , using $\alpha = 3.4 \times (10)^{-5}$ kg/J, $C_1 = 116$, and no work hardening or strain rate hardening adequately fits the loading waves for plate impact velocity of 2210 m/s. Heavier curve is experimental data (Kipp and Grady, 1989). 44

MODELING THE DYNAMIC LOAD/UNLOAD BEHAVIOR OF CERAMICS UNDER IMPACT LOADING

J.R. Furlong, J.F. Davis, and M.L. Alme
R & D Associates

ABSTRACT:

The RDA ceramic failure model was used to model the behavior of SiC and B₄C during plate impact loading. The experiments modeled were performed at Sandia National Laboratory (Kipp and Grady, 1989). The simulations were performed with a version of the Sandia WONDY-V hydrocode (Kipp and Lawrence, 1981) that was modified to run on a PC and to include the RDA ceramic failure model.

The model adequately characterizes the two ceramic materials although B₄C and SiC exhibit distinctly different degrees of work hardening, strain rate hardening, and damage sensitivity. Both materials experienced damage (micro-cracking) on load which was predicted by the model. The experimental unloading data exhibits a reduced magnitude elastic unload wave which suggests that further damage has accumulated after the ceramic reaches peak stress. A strength reducing mechanism such as fatigue or melting at grain boundaries is suspected as the cause of this unpredicted strength loss.

No spall was evident in the measured signals. The model predicts spall will not occur even though the predicted axial stress levels were significantly above the estimated spall strengths of the two ceramics. Failure was prevented by positive (compressive) mean stress levels that were maintained throughout the ceramic specimen during the experimental measurement. A suggested conclusion is that for tensile failure to occur in these ceramics, the mean stress must be negative (tensile).

1. INTRODUCTION:

High-strength ceramics have been shown to be effective armor materials and therefore, the characterization of their dynamic behavior is of great interest. The RDA ceramic failure model (Furlong, Alme and Rajendran, 1988) has been shown to be a valuable tool in simulating ceramics under ballistic impact loading and developing design parameters for armor system design. The modeling of the dynamic load/unload behavior of ceramics under plate impact loading were performed with a version of the Sandia WONDY-V hydrocode (Kipp and Lawrence, 1981) that was modified to run on a PC and to include the RDA ceramic failure model. The major focus of the modeling program has been to model SiC and B₄C plate impact experiments performed at Sandia National Laboratory (Kipp and Grady, 1989).

A systematic approach to modeling these materials was adopted which entails assembly of available Hugoniot data, evaluation of the data to identify a) the underlying hydrostat, b) any unusual strength behavior, c) the effect of porosity on the hydrostat, and d) any evidence of phase transformations. Next, with an assumed hydrostat, the material was modeled as an elastic perfectly-plastic material, then, noting differences between the elastic perfectly-plastic solution and the observed particle velocity history, make adjustments to the RDA model constants for strength and damage until a suitable match was made (or could not be made). Finally, incorporate improvements into the model to reflect new insights of ceramic material properties.

Details of this analysis procedure are described in separate sections of this report. Worthy of note was the unexpected result that none of the ceramics modeled spalled during the period of measurement. This result, predicted by the model, was independent of the impact velocities studied, and occurred at axial tensile stress levels as high as 25 kbar (well beyond the 3-5 kbar range normally associated with spall strength of low porosity, high strength ceramics). Common in all the simulations was the maintenance of a positive (compressive) mean stress (pressure) throughout the specimen that was primarily the result of the close impedance match between the ceramic tiles and the lithium fluoride window of the VISAR instrumentation. Further analysis of the model results indicates that for tensile failure in these ceramics to occur, the mean stress must be negative (tensile).

2. REVIEW OF RDA CERAMIC FAILURE MODEL:

The RDA ceramics failure model is a combined tensile-compressive failure model. The tensile and compressive phases each have their own set of constitutive laws and damage evolution equations. The criterion for branching into either model is the sign of the mean stress (pressure). If at the beginning of each integration cycle the mean stress is positive then the logic for compression is executed. If the mean stress is negative then the logic for tension is executed.

The underlying concept of the tensile model is that of a degraded modulus theory. To implement the theory the usual linear elastic stress-strain equations are modified as

$$P = 3K (1 - D) \phi \quad (1)$$

$$S_{ij} = 2G (1 - D) e_{ij} \quad (2)$$

where P is the pressure (mean stress), S_{ij} and e_{ij} are the deviatoric components of stress and strain, respectively, ϕ is the volumetric strain, K and G are the undamaged bulk and shear modulus of the material, and D is a state variable describing the internal damage in the material. These equations govern the entire elastic and plastic stress response. Concepts such as equations-of-state and yield surfaces do not apply. Hence, the accuracy of the computed stress levels is based on the accuracy of the damage evolution equation.

The tensile damage model is microphysically based and adopts a self-consistent approach to describe the elastic modulus of a cracked body by a crack density (void volume) that is a function of a degraded Poisson's ratio (Budiansky and O'Connell, 1976). When the crack density reaches a level of 9/16, or slightly more than one-half the total volume of an elemental section of material, the modulus is totally degraded and the element ceases to have any stiffness.

The RDA compressive damage model is a plasticity based phenomenological model. Johnson and Cook's (1983) expression for the yield surface of a ductile material has been extended to include a damage softening term, $(1-D)$. The resulting expression for the damaged softened yield surface becomes;

$$Y = ((C_1 + C_2 \epsilon_p^n) (1 + C_3 \ln \dot{\epsilon}^*) (1 - T^{*m}) + C_4 P) (1 - D) \quad (3)$$

where C_1 is the static yield strength, C_2 and n are the strain hardening parameters, C_3 is the viscoplastic (strain rate) parameter, T^* and m are the thermal softening terms, C_4 is the confining pressure parameter, and $(1-D)$ is the damage induced softening term. Therefore, this model can be used to calculate the strength from the combined effects of work hardening, strain rate, thermal softening, and confining pressure. Damage evolution is assumed to be a function of the plastic work rate in compression only. A single damage sensitivity parameter is used to characterize any given materials' dependence of damage on plastic work rate. Under compressive loading, damage affects only the strength of the material, not its stiffness (no change in the longitudinal modulus). However, the combined model maintains a single array for damage, so that damage evolved in tension will affect the strength of the material in compression, and damaged evolved in compression will affect the stiffness of the material in tension.

A more complete description of the model and model theory is included as Appendix 1.

3. MODELING METHODOLOGY:

A systematic approach was used to characterize these materials. The initial step was to assemble all available Hugoniot data, and to evaluate Hugoniot data for identification of a) the underlying hydrostat, b) any unusual strength behavior, c) the effect of porosity on the hydrostat, and d) any evidence of phase transformations. The next step was to model the material as elastic perfectly-plastic with an assumed hydrostat. By noting the differences between the elastic perfectly-plastic solution and the observed particle velocity history, the adjustments were made to the RDA model constants for strength and damage until a suitable match was made (or could not be made). Finally, improvements into the model to reflect new insights of ceramic material properties were incorporated to the model.

If a material behaves in a classic elastic-perfectly plastic manner, a representative load-release path at a position in the target material in uniaxial strain would have the appearance of the path plotted in Figure 1. Note that a reference hydrostat is also included in the figure. The load path is elastic to the Hugoniot elastic limit (HEL) with a slope equal to the longitudinal modulus, ρC_L^2 , where a break in the curve occurs at the HEL and the material behaves as a plastic, and loading continues as defined by the underlying hydrostat, maintaining a separation from the hydrostat of $2/3$ the yield strength. When unloading commences, the material releases elastically, crosses the hydrostat, and continues to unload to a value of $2/3$ the yield strength below the hydrostat with further unloading on a curve as defined by the hydrostat. The paths are characterized by sharp transitions from elastic to plastic states. As discussed in the previous section, the RDA ceramic model assumes damage evolution is a function of the plastic work rate in compression. Thus, above the HEL where the material behaves as a plastic, damage to the ceramic will collapse the Hugoniot to the underlying hydrostat. This effect is shown schematically in Figure 1 with the dashed line.

Above the HEL, the relative contributions of the strength and pressure is not known. The assumption must be made of the form for the hydrostat, then using an appropriate yield function, such as the Johnson-Cook model, make adjustments with the strength model to predict the shape and velocity of the plastic wave. For many materials, the shock velocity u_s may be expressed as a linear function of particle velocity u as given by:

$$u_s = C_o + su_p \quad (4)$$

then

$$P = \frac{\rho C_o^2 \eta}{(1-s\eta)^2} \quad (5)$$

Therefore the hydrostat can be based on a simple shock velocity/particle velocity relation with one free parameter, s , that is used to match the Hugoniot data at high compression (where the strength of the material is assumed negligible). This assumption for the form of the hydrostat assumes a linear function of shock velocity versus particle velocity over the stress-strain space where the stress is the sum of pressure and strength.

Hugoniot data for ceramic materials with porosity indicates that at each initial value of porosity, the ceramic will behave as a different material. This effect is shown schematically in Figure 2. Depending on the initial conditions of the ceramic, the value of the HEL, the longitudinal modulus and the underlying hydrostat can be different. Loss of strength due to damage in the ceramic will collapse the Hugoniot toward the hydrostat of the fully dense ceramic. With incomplete crushing out of porosity, the ceramic will have an unload cold compressive hydrostat determined by the specific volume on unload that is intermediate between theoretical density and the initial density. Energy expended to crush out the porosity will become internal energy and also affect the shape of the hydrostat. Thus, if the porosity is continually changing due to the stress level then the hydrostat would also be continually changing. This effect in ceramics can totally confuse the interpretation of experimental results and is difficult to model accurately.

The effects that the RDA ceramic model has on the particle velocity history are best understood in the context of the idealized load/unload wave profile shown in Figure 3. This figure is a schematic of an experimental planar impact geometry. Position 0.0 is the flyer plate/target plate interface, the left boundary is the flyer plate and the right boundary is the target ceramic/backplate interface. The planar impact produces a compressive wave of uniaxial strain which propagates through both plates. If the flyer and target plate are the same material (as shown in the figure) the wave is symmetric about the impact plane. At high impact velocities, the shock wave will be characterized by a two wave structure. Until the stress in the material reaches its elastic limit (in uniaxial geometry, the HEL) the wave

leading the shock is elastic and travels at the elastic wave speed. This speed is strictly a function of the elastic constants, ρ_0 , C_0 , and v and can be determined prior to the experiment. The time at which this wave arrives at the backplate is used for calibrating of the elastic speed. Above the elastic limit the shock wave is characterized by the second or 'plastic' wave. The arrival time of this wave is dependent upon the strength of the material and the hydrostatic pressure. The shape or profile of the plastic wave front is also determined by the strength and pressure.

The two symmetric elastic and plastic shock waves travel in opposite directions eventually reaching an interface and unloading. The unload is complete (zero stress) if the interface is a free surface. Conversely, if the interface is a perfect impedance match there is total transmission of the wave and no unload wave. Therefore any impedance at the boundary that is comparable to the ceramic impedance will affect the magnitude of the unloading wave. The shape and speed of the unloading wave are equally important for modeling purposes. The wave first unloads elastically. The magnitude of this unload is directly related to the strength of the material and is equal to $4/3 Y$, where Y is the strength. Therefore any difference between the strength used to predict the loading wave and the unloading wave can be ascribed to further 'softening' such as damage that results after load. The second wave is the plastic unloading wave and like the plastic loading wave is dependent on the strength and pressure.

The unloading wave travels in the opposite direction as the loading wave. Because the flyer plate is thinner than the target plate in the experiments modeled, the two unloading waves intersect in the target plate. With totally free surfaces, unlimited strength, and in a lossless medium the magnitude of the stress of these intersecting waves would be negative and twice the shock stress. Normally the material fails (spalls) long before this stress is reached.

For the initial calculations for predicting the measured particle velocity history, a functional form for the hydrostat was assumed, and the ceramic was treated as behaving perfectly plastic. Then the only active parameter in the Johnson-Cook flow stress model is C_1 , the initial yield stress. To choose an initial yield, the well known relationship between dynamic yield and HEL was used:

$$Y_d = \sigma_{HEL} (1 - 2\nu)/(1 - \nu) \quad (6)$$

where

σ_{HEL} = Hugoniot elastic limit

ν = Poisson's ratio

The HEL value was calculated from the particle velocity history at the ceramic/backplate interface by the expression

$$\sigma_{HEL} = \frac{(Z_c + Z_l) u_m}{2} \quad (7)$$

where Z_c and Z_l are the appropriate shock impedance for the ceramic and backplate, respectively, and u_m is the observed particle velocity amplitude selected from each profile which represents the transition from elastic to nonelastic behavior.

As will be shown, for the materials modeled, this approach accurately matched the break point in the velocity history at the HEL and the peak stress level. This approach is normally deficient at predicting 1) the profile of the plastic shock front on load, 2) the magnitude of the elastic unload if the material has softened as a result of compression, and 3) the profile of the plastic unload. It then becomes necessary to make adjustments within the parameter space of the yield function. In this analysis, it was assumed that work hardening, strain rate effects, and damage softening were the relevant parameters to adjust. The effects of thermal softening, and confining pressure, which are also in the model, have not been included in the present analysis. Work hardening is described with a power law function (see equation 3), noting that the exponent characterizes the sensitivity of strength to plastic strain. Variation in the work hardening coefficients has the effect of varying the apparent HEL and increases in work hardening stress will increase the HEL. Consequently, to preserve the HEL indicated by the experimental results, the static yield stress must be reduced. The strain rate term, C_3 , modifies the net strength determined by the initial yield and work hardening terms. Strain rate effects can also increase the HEL and magnitude of the elastic unload. Application of the RDA compressive damage model acts to reduce the strength of the material. Damage softening has been utilized to a) reduce the arrival time of the plastic wave, b) modify the profile of the plastic wave, and c) reduce the magnitude of the elastic unload.

As both the Johnson-Cook model and the RDA compressive damage model are phenomenological, confidence of their accuracy is rooted in their ability to predict results over impact velocity and spatial geometry regimes of interest.

4. THE PC-WONDY COMPUTER CODE:

Since the requirements for computational speed and memory are greatly reduced for problems involving only one dimension it was decided early on in the program to identify a hydro code that would lend itself to easy porting to a PC, allow the implementation of the RDA ceramic model, and be suitable for the types of problems of interest, such as plate impact experiments. The WONDY-V hydrocode is a one-dimensional finite-difference wave propagation code (Kipp and Lawrence, 1981) and was chosen as the vehicle for the modeling effort.

WONDY is comprised of about four thousand lines of FORTRAN making its code core size small, even for a personal computer. WONDY maintains all zonal quantities for all zones in one, singly subscripted array and uses indirect memory access to store and retrieve zonal information. This approach has a number of advantages over codes that maintain zonal quantities in separate arrays. First, it allows for ease of splitting and recombining zones should rezoning be a requirement of a particular problem (e.g. tracking a very steep shock). Second, the size of output "tapes" can be kept small since the data requested for output can be identified by an index (as opposed to placing all variables out on a tape). More importantly, it provides for easy implementation of material models that have an arbitrary number of state variables. WONDY also has available an extensive library of equation-of-state (EOS) routines useful for characterizing a number of solids, gases, and explosives. It is felt that WONDY's treatment of the hydrodynamics and thermodynamics of impact is superior to other available codes. In particular the advantage of using local densities and sound speeds can not be over emphasized when trying to predict accurate deviatoric stress levels and shock propagation velocities.

The environment of the PC provides the user with an extensive array of software utilities, graphics libraries, etc. that can boost both the productivity of code development and quality of graphic output. Making WONDY part of this environment has significantly aided the ability to understand the response of ceramics to dynamic loading.

5. SANDIA PLATE IMPACT EXPERIMENTS:

The experiments selected for simulation were the silicon carbide and boron carbide plate impact experiments recently reported by Kipp and Grady (1989). Note that this report also contains results for titanium diboride and zirconium dioxide. A typical test setup is shown in Figure 4. These impact experiments were symmetric, meaning that the flyer and target plate are the same material. Symmetric impact experiments have the implicit benefit of eliminating any uncertainties associated with the modeling of a second material. However, two other materials necessary for the experiment appear in the figure and must be accounted for when modeling the entire experiment. The first was a foam backing material used to push the flyer plate. Depending on the anticipated flyer velocity, foam with two different densities was used. The lower density foam was 0.32 g/cc and the higher density foam was 0.64 g/cc and was therefore on the order of one-quarter the density of the boron carbide. On the back side of the target plate was mounted a lithium fluoride crystal window. Laser velocity interferometry techniques were used to resolve the longitudinal motion at the ceramic-lithium fluoride interface. Both the density and sound speed of the lithium fluoride are comparable to those of the ceramics modeled and therefore had a significant effect on the magnitude of the transmitted wave through the ceramic-lithium fluoride interface. The interface particle motion versus time was the principal diagnostic of the experiment and the measure by which to judge the accuracy of the model.

Plate dimensions were chosen with two criteria: 1) the release wave coming from the foam-ceramic interface would intersect the ceramic-lithium fluoride release wave in the target plate and 2) release waves from the lateral boundaries of the plates would not reach the axis of measurement until after times of interest. In addition, measurements were made on each ceramic with two flyer plate velocities, designated a low and high velocity. In general the low velocity case was about 1500 m/s and the high velocity case was about 2100 m/s. The particle velocity versus time results for the SiC and the B₄C are shown in Figures 5 and 6, respectively.

6. MODEL RESULTS:

6.1 Ceramic Properties:

The two ceramic materials that were modeled are SiC and B₄C. Table 1 shows the elastic properties for SiC and B₄C (Kipp and Grady, 1989) that were used in the RDA ceramic model. Figure 7 shows the Hugoniot for SiC using LANL data (Marsh, ed., 1980). The solid line is a fit to the data for η greater than 0.15 assuming a linear shock versus particle velocity relationship and represents an assumed shape of the underlying hydrostat from equation 5. The dashed lines represent a classical elastic perfectly-plastic behavior. SiC appears to closely resemble this type behavior from the apparent HEL at 120 kbars to approximately 420 kbars. Note the apparent loss of strength for η values of 0.14 to 0.16 and the collapse to the hydrostat.

The Hugoniot data for B₄C is much more complex. Shown in Figure 8 is Hugoniot data (Gust et al., 1971). Again the solid line is a fit to the data for η greater than 0.15 as was done for the SiC. The dashed lines represent the classical elastic perfectly-plastic behavior. Substantial scatter in the data around the apparent HEL at 150 kbars is observed. The loading curve to the two impact velocities modeled (shown with the vertical dashed lines) is far from plastic behavior and indicates loss of strength and possible changes in the hydrostat.

TABLE 1. CERAMIC PROPERTIES

Material	ρ_0 kg/m ³	C_L km/s	C_s km/s	C_o km/s	ν	σ_{HEL} GPa
SiC	3177	12.06	7.67	8.19	0.16	15.0
B ₄ C	2516	14.04	8.9	9.57	0.164	14.4

6.2 Model Results for SiC:

The low and high velocity impact particle velocity experimental results for SiC are shown in Figure 5. Of the two materials modeled, the silicon carbide more closely resembles a classical elastic-plastic behavior as illustrated in Figure 1. The elastic and plastic shock wave structure and the elastic and plastic unload structure are both readily apparent. An additional wave, most apparent in the high velocity case on load and unload was caused by the wave reflected at the lithium fluoride window. A comparison of the measured and predicted results using a perfectly plastic model for the low and high velocity measurements, respectively, is shown in Figure 9(a & b). This simple model does a remarkably good job of predicting the measured waveforms, particularly in the high velocity impact case.

Both simulations lack the necessary yield function to fill the 'notched' region on load. The perfectly plastic model for the low velocity case over-predicts the level of the plastic unload. The initial hypothesis was that the material spalled and with appropriate adjustment of the tensile damage parameters could be adequately modeled.

Attention was first focused on modeling the obvious features of load and elastic unload by variation of the strain rate, strain hardening and damage coefficients. Figure 10(a-d) shows a progression of computations varying only the strain rate coefficient, C_3 for the high velocity case. Choosing a value of .02 for C_3 appears to yield an excellent match to the observed velocity versus time profile for features related to the load and elastic unload. But there are subtle features that cannot be matched with strain rate alone. This choice for C_3 removed too much of the corner at the loading peak. Also, the magnitude of the elastic unload is too large. The unload wave arrives too early, suggesting that a dispersive mechanism has occurred in the plate. Finally, even though the plastic unload level appears correct there was an anomalous wave that arrives at 1.7 μ s.

Figure 11(a-d) shows the collective effort of many calculations resulting in choices for all parameters that in an overall sense yield the best fit to the load and the elastic unload features of the high velocity data. In order, the progression is from perfectly plastic with an initial yield value of $C_1 = 80$ kbar, to the addition of 75 - 80 kbar of work hardening using values $C_2 = 100$, $n = 0.1$, to the addition of 6 - 8 percent compressive damage using a value $\alpha = 0.7 \times (10)^{-6}$ (kg/J), to the addition of a strain rate coefficient of 0.008. Both work

hardening and strain rate have the effect of filling in the 'notched' region seen in the perfectly plastic case. However, strain rate tends to overfill this region near the HEL and under fill the region at the peak. The work hardening function fills this region more uniformly and overall allows for more accurate matching to the profile of the plastic wave.

In all cases the unloading wave arrives too soon. In order to match this arrival it was necessary to modify the isentrope during unload. The conventional approach to using a Mie-Gruniesen EOS in a hydro code is to unload along the load isentrope. It should be noted that the velocity histories reported by Kipp and Grady indicated significant dispersion observed in the unload for boron carbide, titanium diboride, and zirconium dioxide materials with SiC indicating somewhat less dispersion. If the unload isentrope was taken along a path to a lower density than the original density at zero pressure then a suitable match with the SiC could be made. PC-WONDY was modified to allow specification of an arbitrary pressure offset at zero strain during unload. Without suitable theory to support such an effect caution has been exercised before using this option. However, the model results are improved when a 30 kbar offset at zero strain was used as shown in Figure 12 which compares the model with the measurement.

Shown in Figure 13 is the comparison between the model prediction and the low velocity measurement using the same parameters as in the high velocity case. These results compare favorably with the experimental data for the first and second shock wave on load, and the arrival time of the elastic unload wave. However, the calculation predicts only elastic unload whereas the measurement shows a plastic, highly dispersive wave at 1.35 μ s.

The arrival of the additional wave at 1.7 μ s and the modest dispersive unload wave in the high velocity case and the highly dispersive unload wave in the low velocity case were all originally thought to be a spall phenomenon that could be modeled by suitable adjustment of the tensile damage model parameters. Figure 14 is used to show the characteristic particle velocity history that occurs when a material spalls. The abrupt change in slope seen in the figure is not observed in either the low or high speed impact particle velocity measurements suggesting the material either has no spall strength or does not spall and some other event was responsible for the wave structure. Further, the model predicted no spall, regardless of the magnitude of the tensile model damage sensitivity parameters. Closer examination of the

calculation revealed that the mean stress (pressure) remained positive (compressive) throughout the entire calculation. Figure 15 shows the pressure distribution when the pressure reaches its absolute minimum in the target plate. Since the tensile model is activated by a negative pressure, no tensile damage was calculated. The ceramic maintained this compressive state for three reasons: 1) the impedance of lithium fluoride was sufficiently close to the ceramic target to allow transmission of a major fraction of the pressure component of the shock wave (using the computed peak particle velocities and equations (2-7) to (2-9), the impedances of the silicon carbide and lithium fluoride are 4.3×10^7 and 1.62×10^7 rayls, respectively), 2) 30 percent of the pressure was transmitted into the foam backing material, and 3) energy was deposited in the plates that acts to reduce the strength of the ceramic either through damage (micro-cracking) or thermal melting. For the modeled impact velocities, removal of the lithium fluoride window is sufficient to produce negative pressure in the target and cause spall. For comparison, Figure 16 shows the pressure distribution for the high velocity case when the lithium fluoride window has been removed from the calculation. Note the signature of a spall zone at a position 6 to 7 mm from the flyer/target plate interface.

If the material indeed does not spall then another explanation is required for the wave structure near $1.7 \mu\text{s}$ after plate impact. Further investigation with variation of the boundary conditions at interfaces including removing the foam material from the calculation revealed that the arrival time of the anomalous wave was coincident with the arrival of a wave caused by an event occurring at the boundary of the foam-ceramic interface immediately after unload. This result lead to the conclusion that the observed wave form is not a spall signal and supports the model result that the target ceramic did not spall. Therefore, some modification to the damage model is necessary to produce the observed events associated with unload in the flyer.

The comparison between the model prediction and measured particle velocity for the low impact SiC shows that the model over-predicts plastic unload whereas the measurement shows a highly dispersive plastic unload wave. Like the high speed case the low speed case does not show the characteristic spall signal as illustrated in Figure 14. The unload level is directly related to the amount energy released during unload i.e. energy transmitted into the

foam or dissipated in the flyer or target will tend to reduce the amount of unload increasing the particle velocity level. Since energy lost to micro-cracking is known to reduce the magnitude of the elastic unload, the compressive damage model can be used as a device to reduce the strength of the material, beyond what was necessary to match load, to see what effect this would have on the unload particle velocity history. Figure 17(a - d) shows the progression of results when α was systematically increased. Figure 18 compares the experimental measurements with the model results using an $\alpha = 0.32 \times (10)^{-5}$ (kg/J) which best matches the elastic unload. This value of damage sensitivity results in damage in the target plate of 40 percent. Obviously increasing α ruins the predicted performance for load. Since both the load and unload waves cannot be matched with the same value of α and since the load can be correctly predicted, then damage or some other strength reducing mechanism was taking place after load while the material was at peak stress or even as it unloads. Candidate theories are fatigue, melting at grain boundaries of the ceramic and conversion of internal energy to micro-crack growth and coalesce. Since the model predicts the high speed impact adequately without introducing additional damage, the additional damage may be inversely related to impact speed. This suggests a confining pressure effect, or other crack growth mitigating effect such as ratio between pressure and deviatoric stress.

Silicon carbide has been successfully modeled with the RDA ceramic failure model with the Johnson-Cook flow stress model modified by damage softening. Within the context of this model SiC exhibits about 75-80 kbar of work hardening. A compressive damage sensitivity of $0.7 \times (10)^{-6}$ (kg/J) produced 6-8 percent and 12 - 15 percent strength reduction on load in the low and high velocity impact cases, respectively. Some strain rate dependence was required to smooth certain portions of the velocity history. It was also necessary to prescribe a separate unloading isentrope with a pressure offset of 30 kbar to match the arrival time of the unload wave in the high speed case.

Model predictions made a satisfactory match with experiment for load, but over-predicted the magnitude of unload for the low speed impact case. After loading, increasing the calculated damage from the predicted level of 6 - 8 percent to 40 percent while the material was at peak stress was necessary to match the unload particle velocity history.

6.3 Model Results for B₄C:

The approach to modeling B₄C begins with an examination of the available Hugoniot data. Figure 19 is stress versus η for B₄C from planar impact experiments (Gust, et al, 1971). The solid line is a fit to the data for η greater than 0.15 and is the shape of the hydrostat assuming a linear relationship between the shock velocity and the particle velocity (equations 6 and 7). The observed $\Delta\eta$ at constant stress for $\eta = 0.055$ to .065 is indicative of possible loss of porosity or phase change in the ceramic. The shape of the underlying hydrostat was therefore unknown and the load and unload paths would be different.

The low and high velocity impact particle velocity experimental results are shown in Figure 6. Unlike the SiC, B₄C exhibits a number of differences distinguishing its behavior from the ideal elastic-plastic behavior shown in Figure 3. First, the HEL is marked by uncharacteristic oscillations. Kipp and Grady account for this behavior as a "heterogeneous failure or faulting mechanism during compressive loading coupled with the small laser spot size associated with VISAR measurements." No better explanation is apparent, nor does the model attempt to predict it. Instead, values for the yield parameters values have been chosen that best fit the mean of the oscillatory behavior. Second, completely absent in the particle velocity measurement of the low speed impact case was any evidence of elastic unload. In the classical case there is always a linear non-dispersive unloading path. This absence of elastic unload suggests a total loss of strength. Third, the entire unloading path was dispersive and cannot be accounted for by the hydrostatic model used during load. This suggests that the material has substantially changed in character, perhaps undergoing phase or phases of transformation and/or as with SiC, the material has additional damage or other strength reducing mechanism that was taking place after load while the material was at peak stress or even as it unloads.

In the low impact velocity measurement, a dip was observed immediately following the arrival of the plastic wave when one normally expects to see a plateau. Although it is not unusual behavior, the markedly higher sound speed of the B₄C created some modeling diagnostic difficulty in the context of the plate thicknesses and impact velocities used in the experiments. The combination of a slow plastic loading wave (caused by considerable damage) and fast elastic unloading wave allowed the unloading wave to overtake the loading

wave at approximately the VISAR location. This event was further complicated by the wave reflecting at the ceramic-lithium fluoride interface.

Shown in Figure 20 is a comparison of the measured and predicted results using an elastic perfectly-plastic model for the low velocity impact case. The model can adequately predict the HEL, but the similarity ends there. In the perfectly plastic model the plastic shock arrival time was too early. The measurements clearly indicate a transition from an elastic to a perfectly plastic wave. The addition of damage with the compressive damage model was then used to delay the arrival of the plastic shock. Figure 21(a-d) shows the predicted waveforms after making adjustments of the compressive damage sensitivity parameter, α (see equation 1 - 20) for the low velocity impact case. Note in the figures that as α increases, the arrival time of the plastic shock was delayed. The elastic unloading wave, whose arrival time will not vary (so long as the material retains some elasticity), begins to catch up to the plastic load, eventually overtaking it in Figure 21(d).

Figures 22 and 23 show the comparison between the model predictions and the measured particle velocity histories for both the low and high velocity cases. These results were obtained using a damage parameter of $\alpha = 3.4 \times (10)^{-5} \text{ kg/J}$ and produces a good fit to the observed loading waveforms. The level of damage computed as a result of the compressive shock was between 45 - 50 percent, and 65 - 70 percent for the low and high velocity cases, respectively. As mentioned earlier, the measurements for the low and high velocity impact experiments indicate highly dispersive unloading waves. The low speed impact case shows no evidence of any elastic strength after being compressed. The small linear segment at the beginning of unload in the high speed impact case was believed to be evidence of the residual strength of the ceramic. Using the length of this segment, the measured particle velocity and equations (2 - 7) to (2 - 9), implies a residual strength of 15.4 kbar, implying damage of 87 percent in the ceramic. The linear segments at the beginning of unload in the low and high speed plate impact model predictions indicates that the material in the two experiments should have more strength than was observed.

Boron carbide has been successfully modeled by the RDA ceramic failure model with the Johnson-Cook flow stress model modified by damage softening. B_4C exhibits little or no work hardening, and no significant strain-rate dependence. Using a value of $\alpha = 3.4 \times (10)^{-5}$

kg/J provides a good fit to the measured loading waves for both low and high velocity cases. The level of damage computed as a result of the compressive shock was between 45 - 50 percent, and 65 - 70 percent for the low and high velocity cases, respectively. Dispersive unloading with little evidence of an elastic unload are required to predict the experimental data suggesting either damage reduced modulus or non-zero pressure on return to original density. Removing the strength from the ceramic in the model predictions to match the unload profile affects the good match with the load profile and leads to the same conclusion that was reached with the SiC. Damage or some other strength reducing mechanism was at work after load, decreasing the strength of the ceramic more than was necessary to accurately predict load. A further similarity between the two materials was that the damage appears to be more severe at the low impact velocity than at the high impact velocity.

7. SUMMARY

The RDA ceramic failure model was used to model the behavior of SiC and B₄C during plate impact loading. Experiments modeled were those of Sandia National Laboratory (Kipp and Grady, 1989). The simulations were performed with a PC based version of the Sandia WONDY-V hydrocode (Kipp and Lawrence, 1981). WONDY-V was converted to a 386 PC, and then the RDA ceramic failure model was incorporated into it.

The model characterized the two ceramic materials with distinctly different work hardening, strain rate, and damage sensitivity. Within the context of the model SiC exhibited 75 - 80 kbar work hardening and some strain rate sensitivity. A compressive damage sensitivity of $0.7 \times (10)^{-6}$ (kg/J) produced 6-8 percent and 12 - 15 percent strength reduction on load in the low and high velocity impact cases, respectively. Some strain rate dependence was required to smooth certain portions of the velocity history.

Model predictions for SiC made a satisfactory match with experiment for load, but over-predicted the magnitude of unload for the low speed impact case. After loading, increasing the calculated damage from the predicted level of 6 - 8 percent to 40 percent while the material was at peak stress was necessary to match the unload particle velocity history.

In contrast to SiC, B₄C exhibits little or no work hardening, and no significant strain-rate dependence. Using a value of $\alpha = 3.4 \times (10)^{-5}$ kg/J provides a good fit to the measured loading waves for both low and high velocity cases. The level of damage computed as a result of the compressive shock was between 45 - 50 percent, and 65 - 70 percent for the low and high velocity cases, respectively. Dispersive unloading with little evidence of an elastic unload is required to predict the experimental data suggesting either damage reduced modulus or non-zero pressure on return to original density.

For both ceramics, particle velocity histories indicate that, after loading, further damage occurs and is inversely related to impact velocity. When damage is allowed to increase beyond the level required to adequately match the loading profile, a suitable match with the unloading profile can be made. This additional damage which cannot be predicted with the current model suggests other strength reducing mechanisms are at work while the ceramic was at peak stress or at unload. Candidate theories for this behavior are fatigue

and/or thermal melting at the grain boundaries of the ceramic. Lack of additional damage evolution in the high speed impact case suggests its cause may be mitigated by confining pressure or ratio of pressure to deviatoric stress effects.

Positive (compressive) mean stress levels were maintained throughout the test specimen during the experimental measurement as a result of the boundary conditions provided by the lithium fluoride window of the VISAR instrumentation and the flyer plate foam backing material. Energy absorption as a result of compressive damage and/or melting at the grain boundaries also contributes to the maintaining of positive mean stress levels. The predicted axial stress level in the high impact velocity case for SiC was approximately 25 kbar which is well above the 3-5 kbar range normally associated with the spall strength of low porosity, high strength ceramics, however, no spall was evident in the experimentally measure signals and the model predicts no spall to occur. Therefore, these results support the hypothesis that for tensile failure in these ceramics, the mean stress must be negative (tensile). This result, if true, would have a significant impact on the design of armor. A major design issue would be whether or not the ceramic is confined, not the level of confining pressure.

THE VIEWS, OPINIONS, AND/OR FINDINGS CONTAINED IN THIS REPORT ARE THOSE OF THE AUTHORS AND SHOULD NOT BE CONSTRUED AS AN OFFICIAL DEPARTMENT OF THE ARMY POSITION, POLICY, OR DECISION, UNLESS SO DESIGNATED BY OTHER DOCUMENTATION.

REFERENCES:

1. B. Budiansky, R.J. O'Connell, "Elastic Moduli of a Cracked Solid," *International Journal of Solids Structures*, Vol. 12, pp. 81-97, 1976.
2. J.R. Furlong, M.L. Alme, and A.M. Rajendran, "A Combined Tensile/Compressive Failure Model for Brittle Materials Applied to the Penetration of Ceramic Targets by LRP's", *Proceedings of the Fifth TACOM Armor Coordinating Conference for Light Combat Vehicles*, Naval Postgraduate School, March 1989.
3. J.R. Furlong, M.L. Alme, and A.M. Rajendran, "Numerical Modeling of Ceramic Penetration Experiments", *Proceedings of the Fourth TACOM Armor Coordinating Conference for Light Combat Vehicles*, Naval Postgraduate School, March 1988.
4. L.A. Glenn, "The Calculation of Brittle Fracture in Rock-like Media, I. Spherical Wave Propagation in Glass", *CERAC Report No. 22*, Project No. 215, Mar 6, 1974.
5. D. Grady, "The Mechanics of Fracture under High-rate Stress Loading," in: A.P. Bazant, ed., *Preprints of the William Prager Symposium on Mechanics of Geomaterials: Rocks, Concretes and Soils*, Northwestern University, Evanston, IL, 1983.
6. D.E. Grady and M.E. Kipp, "Dynamic Rock Fragmentation," *Technical Report: SAND84-2456J*, Sandia National Laboratories, Albuquerque, NM, December 1984.
7. W. H. Gust and E. B. Royce, "Dynamic Yield Strengths of B_4C , BeO , and Al_2O_3 Ceramics," *Jour. of Appl. Phy.*, Vol 42, Number 1, Jan 71, p 276.
8. W. Herrmann, R.J. Lawrence, and D.S. Mason, "Strain Hardening and Hardening and Strain Rate in One-Dimension Wave Propagation Calculations" *Sandia Laboratories*, SC-RR-70-471, November 1970.
9. G.R. Johnson and W.J. Cook, "A Constitutive Model and Data for Metals Subjected to Large Strains, High Strain Rates and High Temperatures," *Proceedings of Seventh International Symposium on Ballistics*. The Hague, The Netherlands, April 1983.
10. G.R. Johnson and R.A. Stryk, "User Instructions for the EPIC-2 Code", *AFATL-TR-86-51*, August 1986.
11. M.E. Kipp and D.E. Grady, "Shock Compression and Release in High Strength Ceramics", *SAND89-1461*, Jul 1989.

12. M.E. Kipp and R.J. Lawrence, "WONDY V - A One-Dimensional Finite-Difference Wave Propagation Code", SAND81-0930, Unlimited Release, Printed June 1982.
13. E. Lee, M. Finger, and W. Collins, "JWL Equation of State Coefficients for High Explosives", Lawrence Livermore Laboratory, UCID-16189, January 1973.
14. LOS ALAMOS SERIES ON DYNAMIC MATERIAL PROPERTIES, Stanley P. Marsh, ed., Univ. of Cal. Press, 1980. ISBN 0-520-04007-4.
15. L.N. Taylor, E.P. Chen, and J.S. Kuszmaul, "Microcrack-Induced Damage Accumulation in Brittle Rock under Dynamic Loading," Computer Methods in Applied Mechanics and Engineering, 55, 1986.

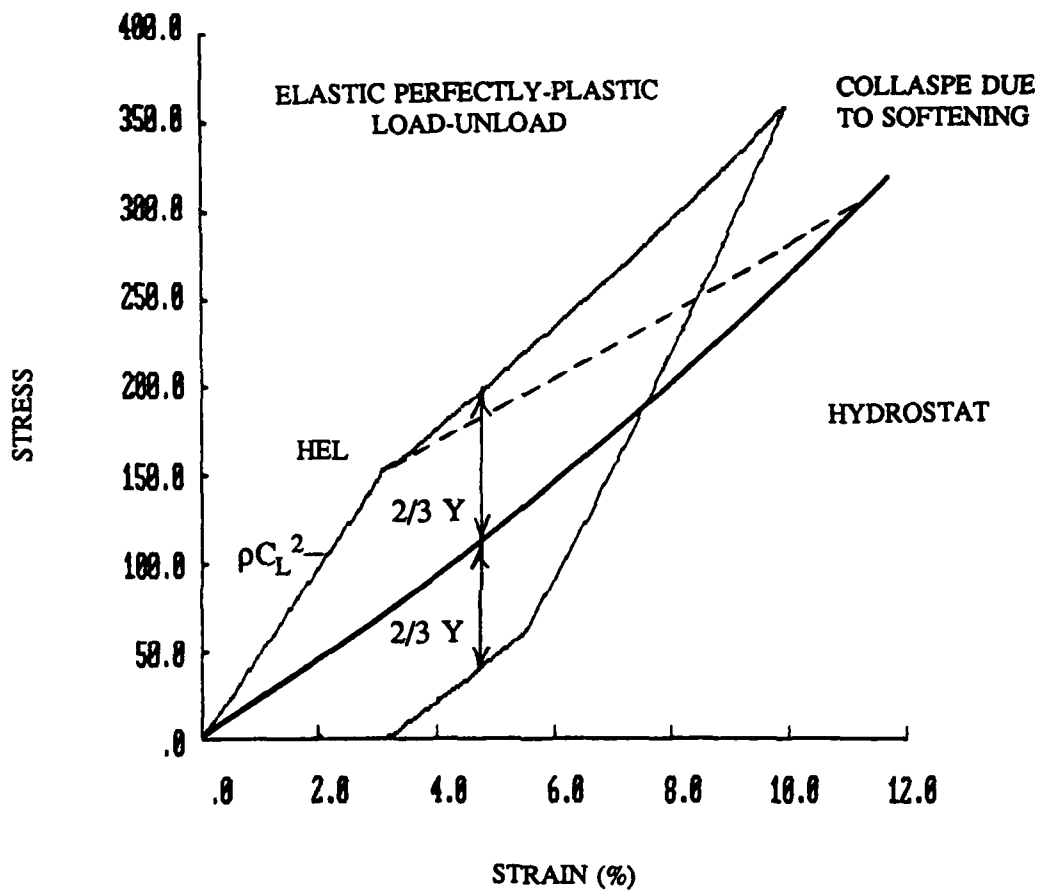


FIGURE 1: Elastic perfectly-plastic stress-strain path showing relationship to the hydrostat (heavy line). Dashed line illustrates response with softening such as damage.

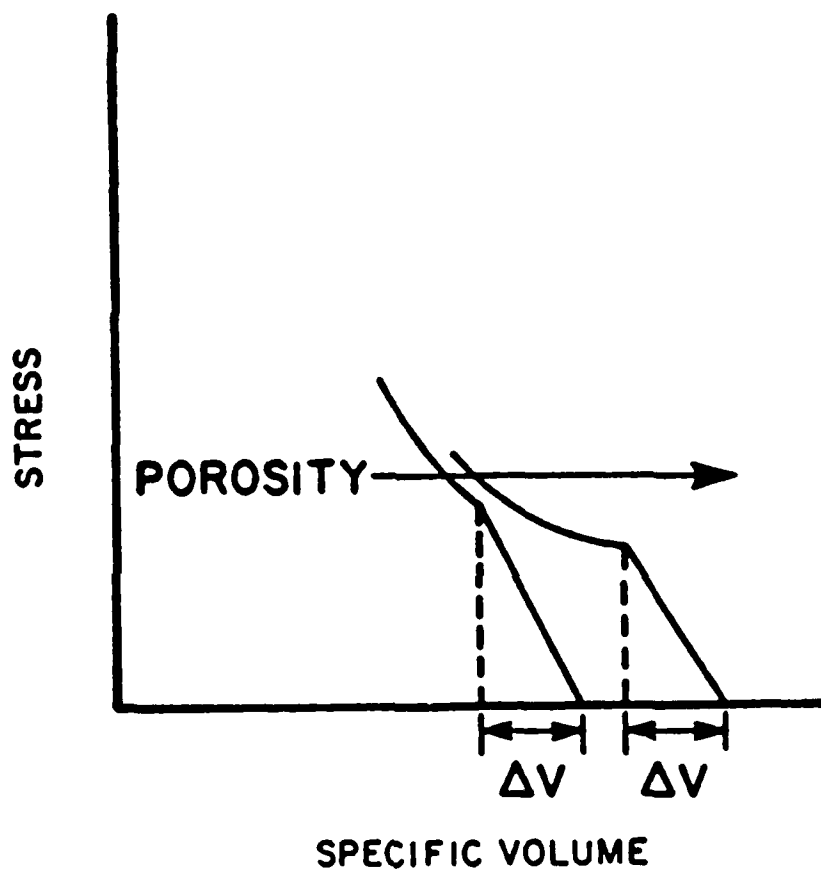


FIGURE 2: Schematic of Hugoniot for a ceramic material with porosity indicating that at each initial specific volume, the material will have a different HEL and potentially different longitudinal modulus. Loss of strength due to damage in the material collapses the Hugoniot toward the hydrostat of the fully dense material.

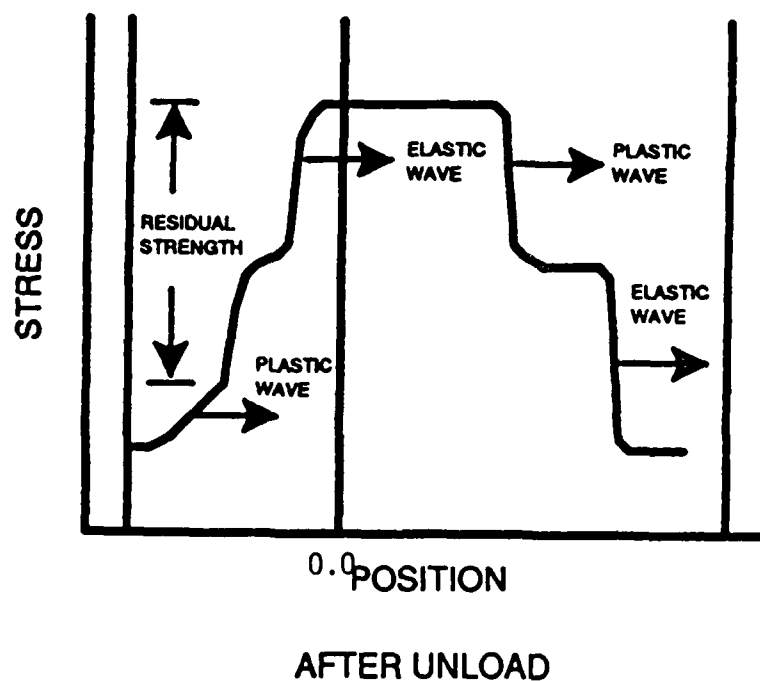
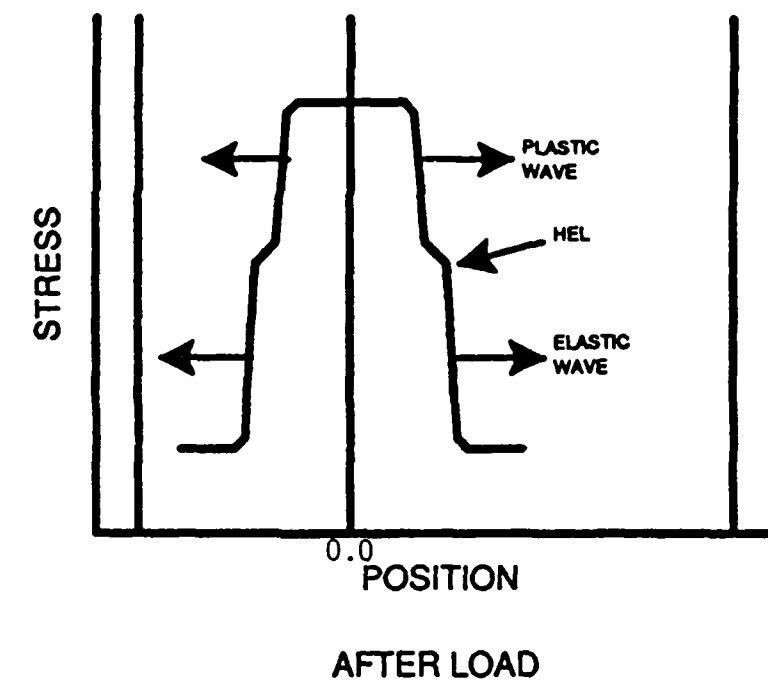


FIGURE 3: Idealized load/unload wave profiles for planar impact experiments.

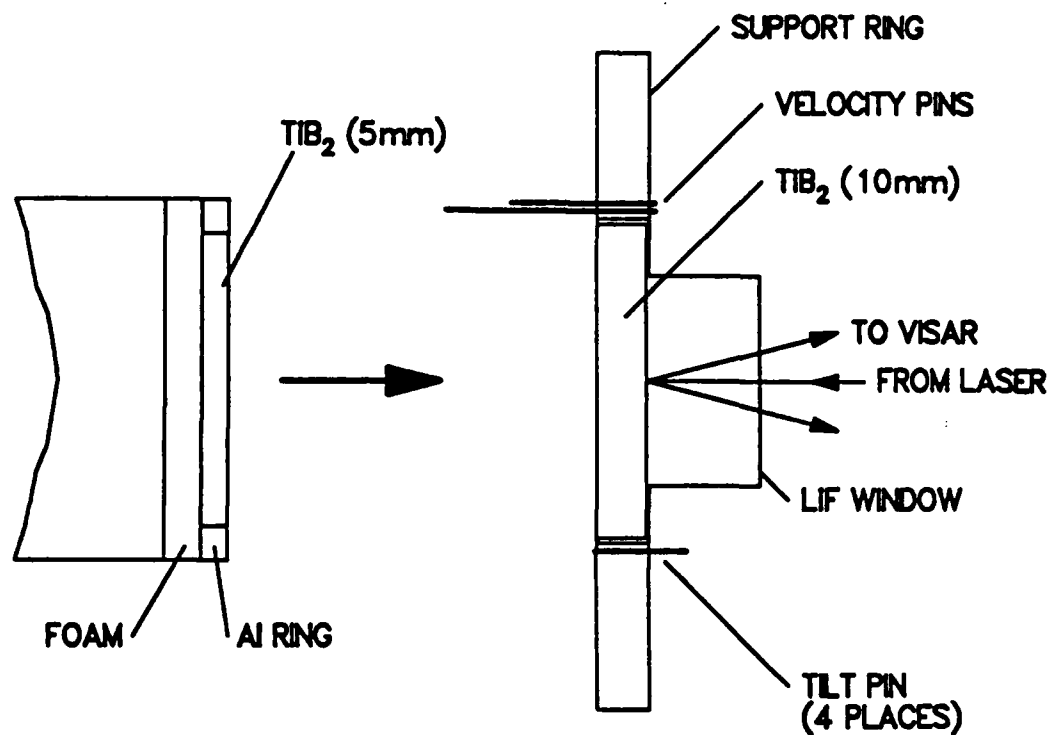


FIGURE 4: Plate impact experimental configuration of Sandia National Laboratory experiments (Kipp and Grady, 1989).

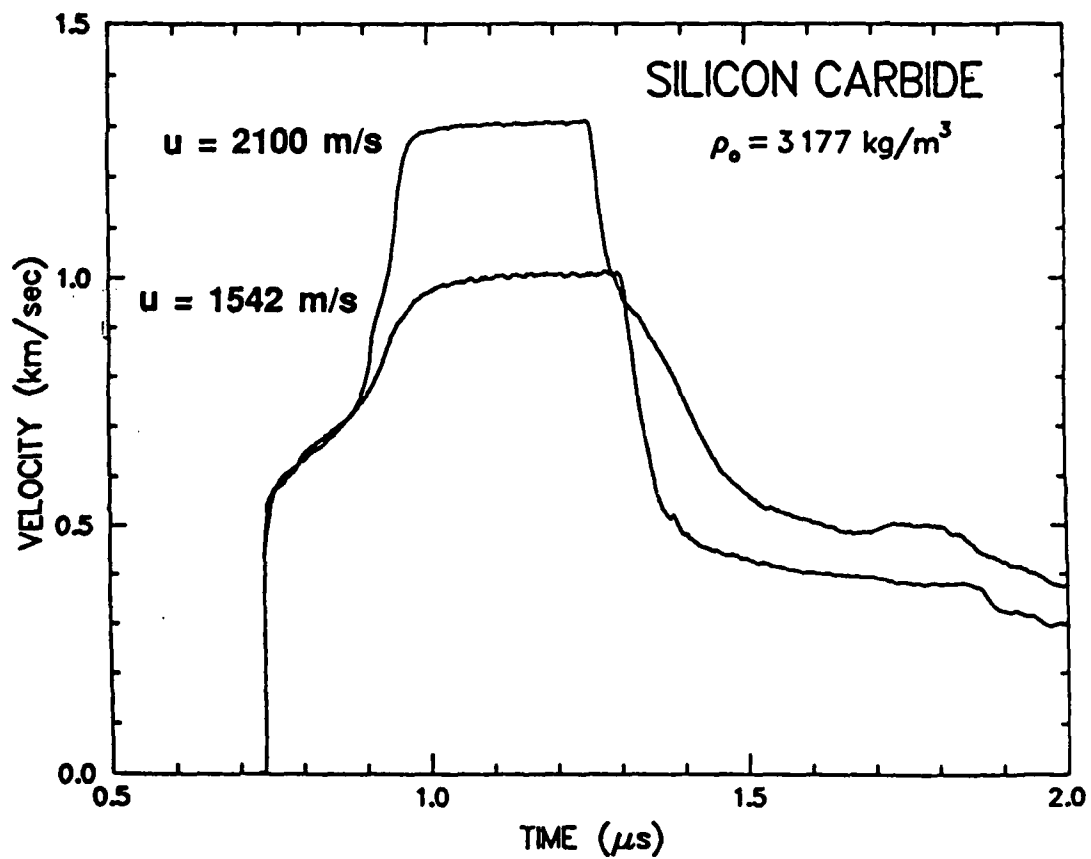


FIGURE 5: Experimental results for SiC for plate impact velocities as indicated using the experimental configuration of Figure 8 (Kipp and Grady, 1989).

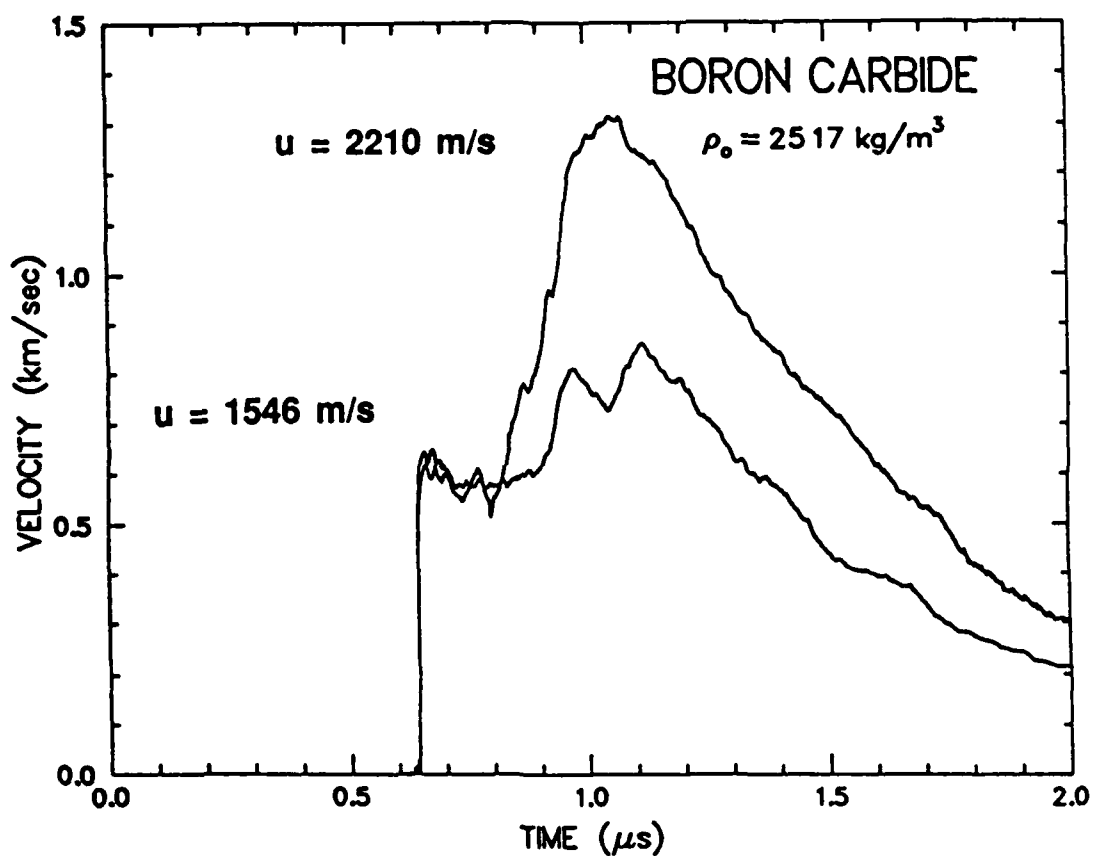


FIGURE 6: Experimental results for B_4C for plate impact velocities as indicated using the experimental configuration of Figure 8 (Kipp and Grady, 1989). Note the dispersive unload behavior and absence of apparent strength on unload.

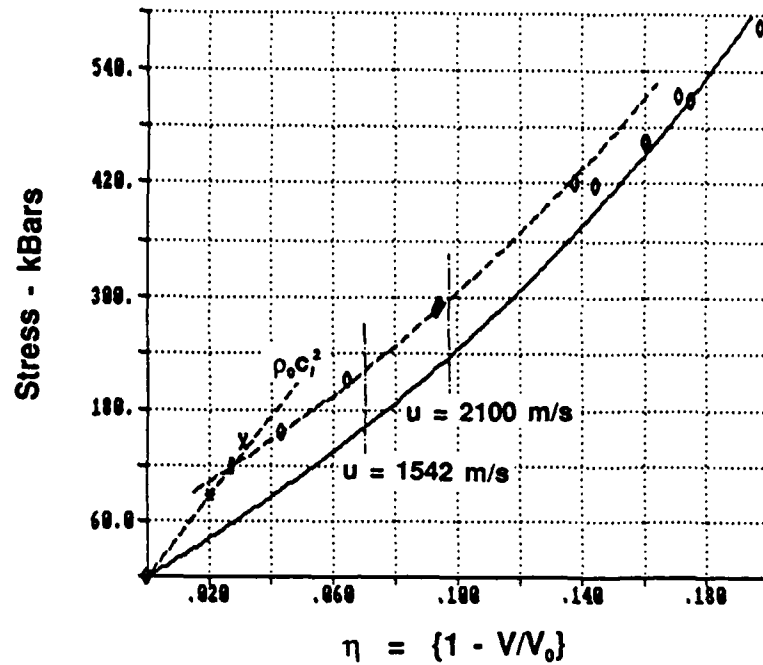


FIGURE 7: Least squares fit to Hugoniot data for SiC (LANL, 1980) using equation 5 for η values greater than 0.15 (solid line). The dashed line represent elastic perfectly-plastic behavior.

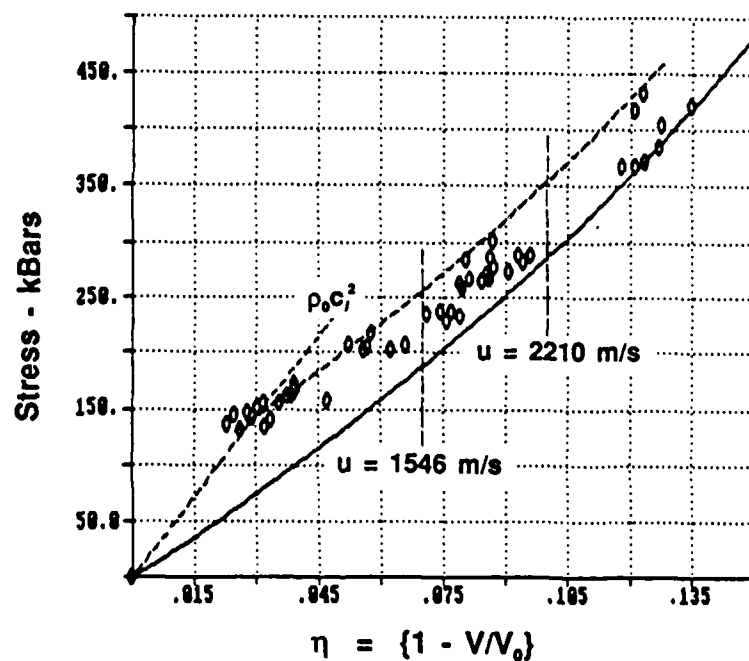


FIGURE 8: Least squares fit to experimental Hugoniot data for B_4C (Gust et al, 1971) using equation 5 for η values greater than 0.15 (solid line). The dashed lines represent elastic perfectly-plastic behavior.

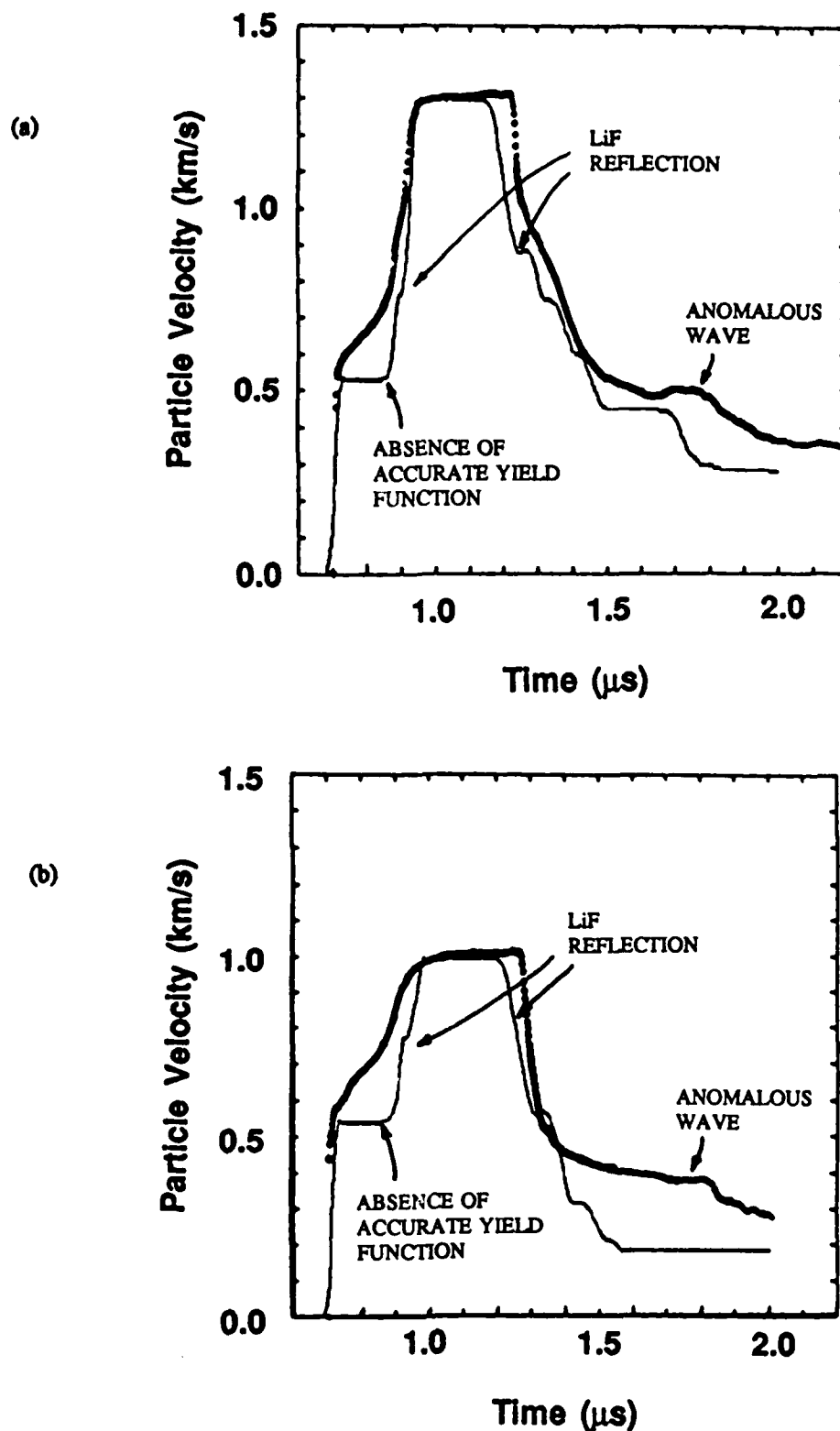
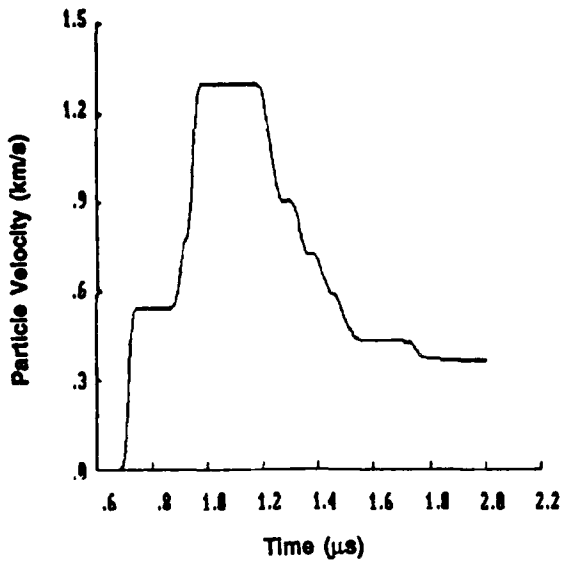
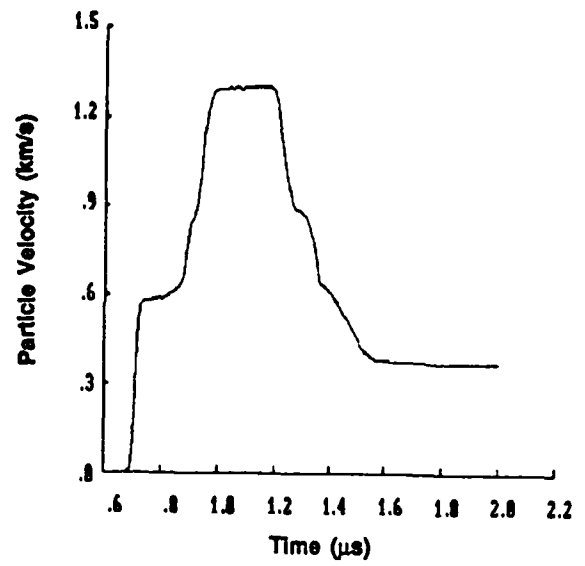


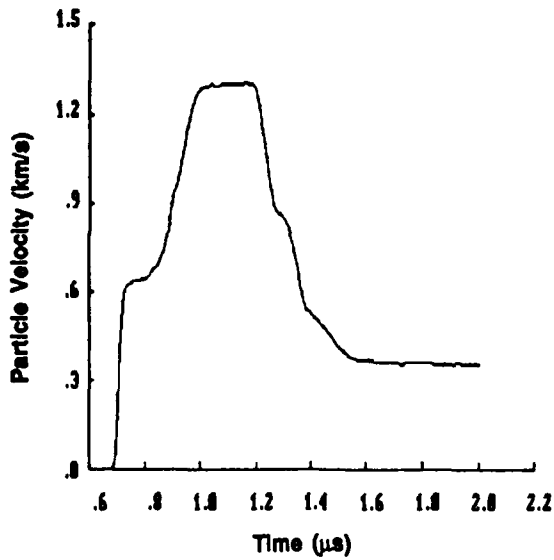
FIGURE 9: Comparison of PC-WONDY model predictions and experimental data (Kipp and Grady, 1989) for SiC using an elastic perfectly-plastic model; (a) for plate impact velocity of 2100 m/s and (b) for plate impact velocity of 1542 m/s. This model shows clearly an absence of accurate yield function, the reflection of the LiF window and the presence of an anomalous wave at approximately 1.7 μ s.



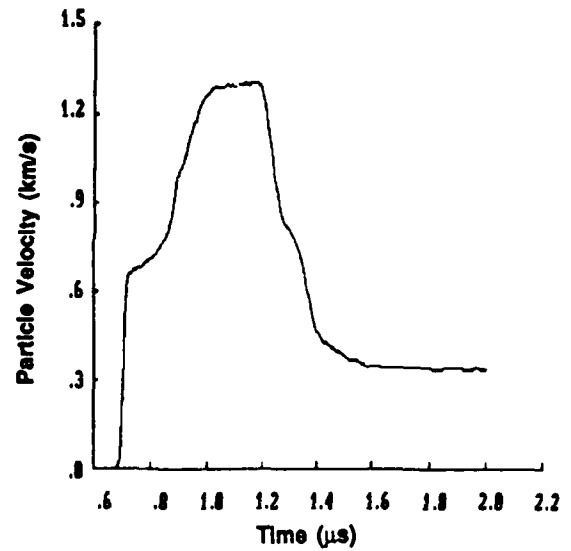
(a) Perfectly-plastic



(b) $C_3 = 0.01$

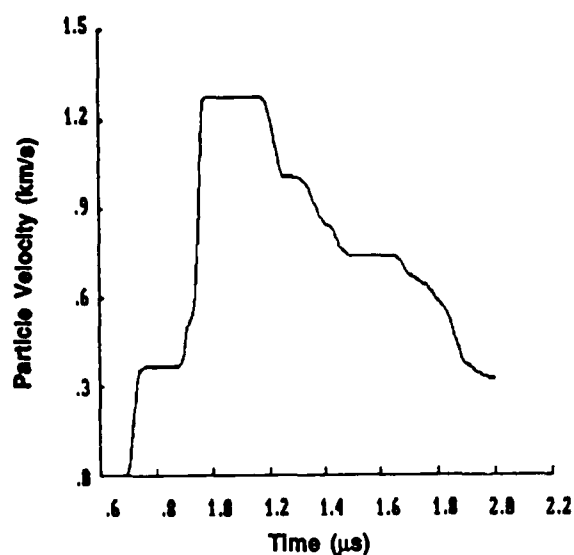


(c) $C_3 = 0.02$

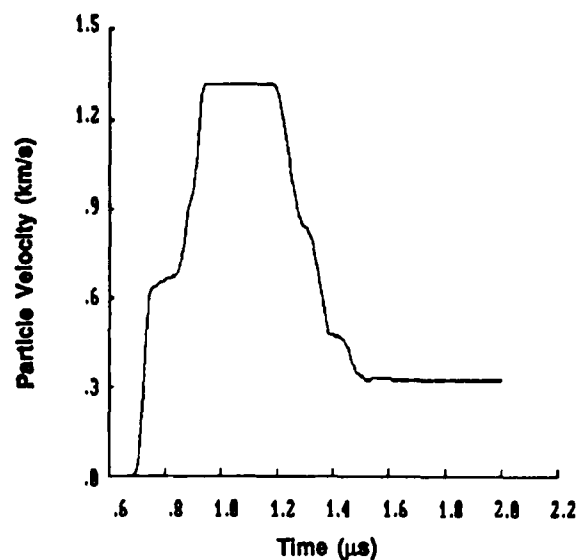


(d) $C_3 = 0.03$

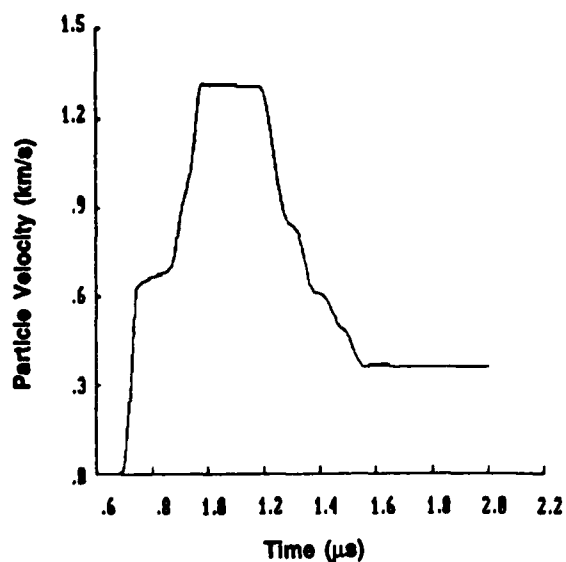
FIGURE 10: Model predictions for 2100 m/s plate impact experiments with SiC with an increase in the strain rate hardening term, increases the apparent HEL, increases the magnitude of the elastic unload and causes the unload wave to arrive earlier.



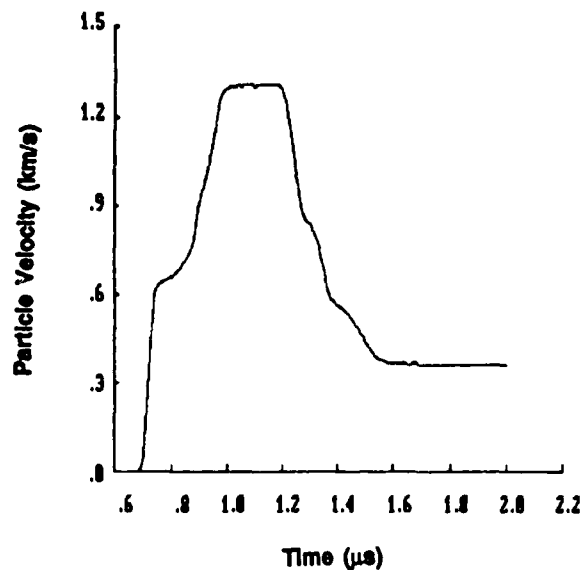
(a) $C_1 = 80$ kbar



(b) $C_1 = 80$ kbar, $C_2 = 100$ kbar, and $n = 0.1$



(c) $C_1 = 80$, $C_2 = 100$, $n = 0.1$,
 $\alpha = 0.7 \times 10^{-6}$ kg/J



(d) $C_1 = 80$, $C_2 = 100$, $n = 0.1$,
 $\alpha = 0.7 \times 10^{-6}$ kg/J and $C_3 = 0.008$

FIGURE 11: A systematic variation of initial yield, strain hardening parameters, strain rate hardening and damage coefficients for SiC yields a good fit for the load and elastic unload for planar impact experiments (Kipp and Grady, 1989) for impact velocity of 2100 m/s.

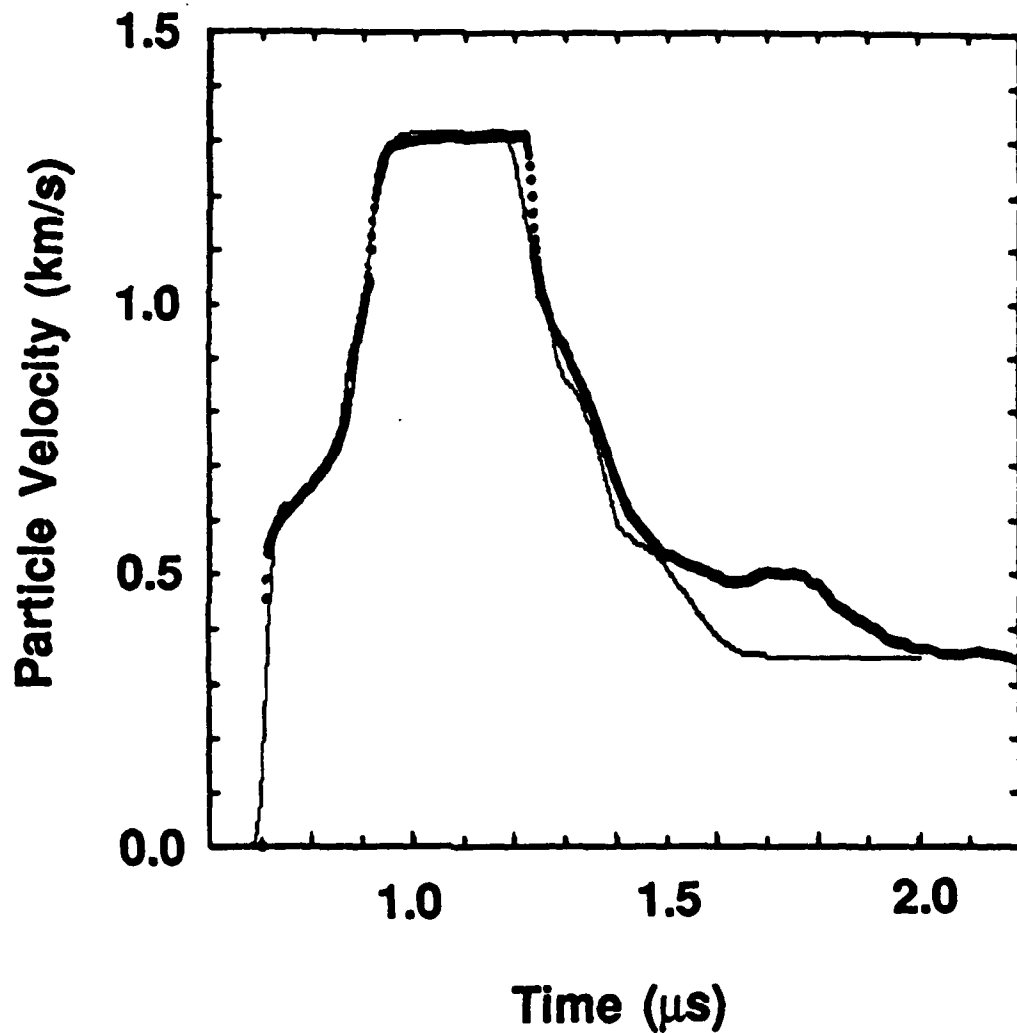


FIGURE 12: Comparison of PC-WONDY model predictions with experimental results for SiC with plate impact velocity of 2100 m/s using the parameters $C_1 = 80$, $C_2 = 100$, $n = 0.1$, $\alpha = 0.7 \times 10^{-6}$ kg/J, and $C_3 = 0.008$ with the unload isentrope having 30 kbar offset at zero strain. As shown, these results compare favorably with the experimental data (Kipp and Grady, 1989).

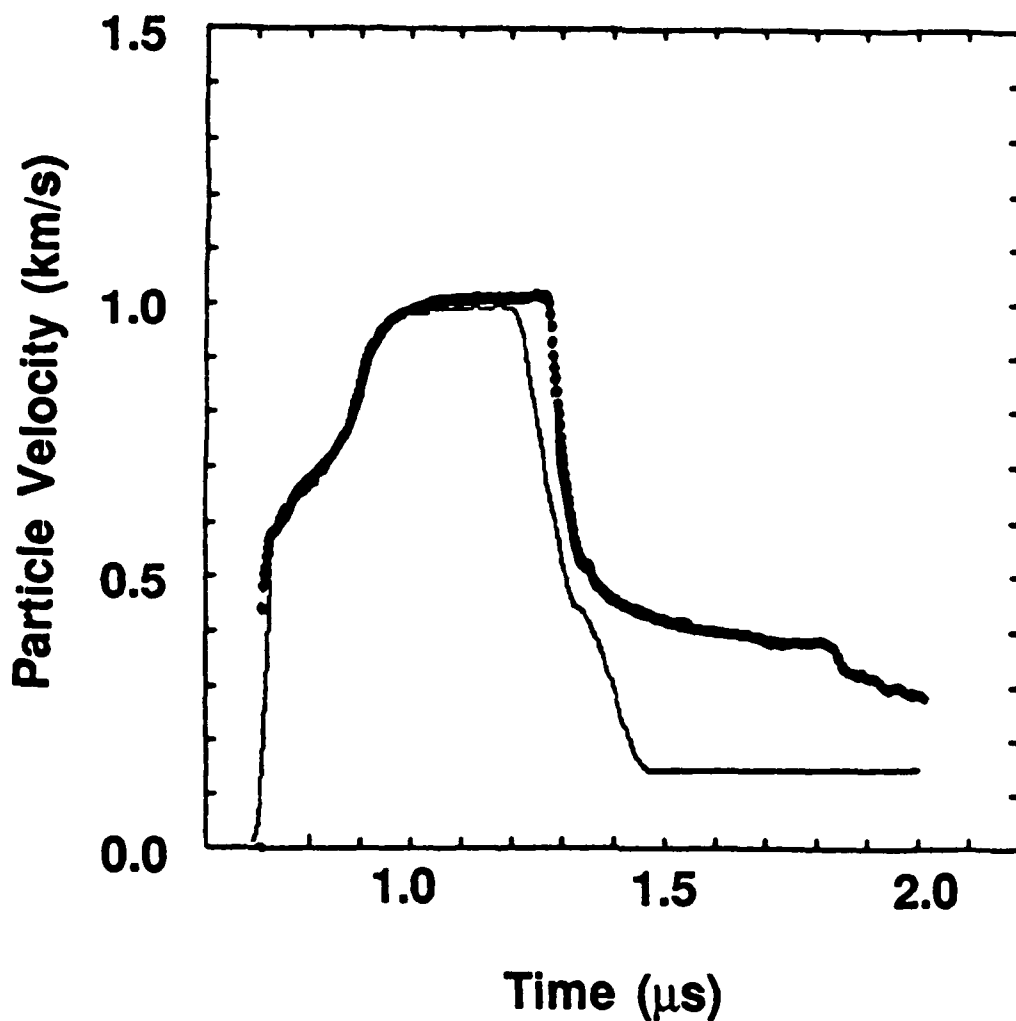


FIGURE 13: Comparison of PC-WONDY model predictions with experimental results for SiC with plate impact velocity of 1540 m/s using the parameters $C_1 = 80$, $C_2 = 100$, $n = 0.1$, $\alpha = 0.7 \times 10^{-6} \text{ kg/J}$, and $C_3 = 0.008$ with the unload isentrope having 30 kbar offset at zero strain. As shown, these results compare favorably with the experimental data (Kipp and Grady, 1989) for 1.2 microseconds after plate impact (loading waves), but does not model the unload adequately.

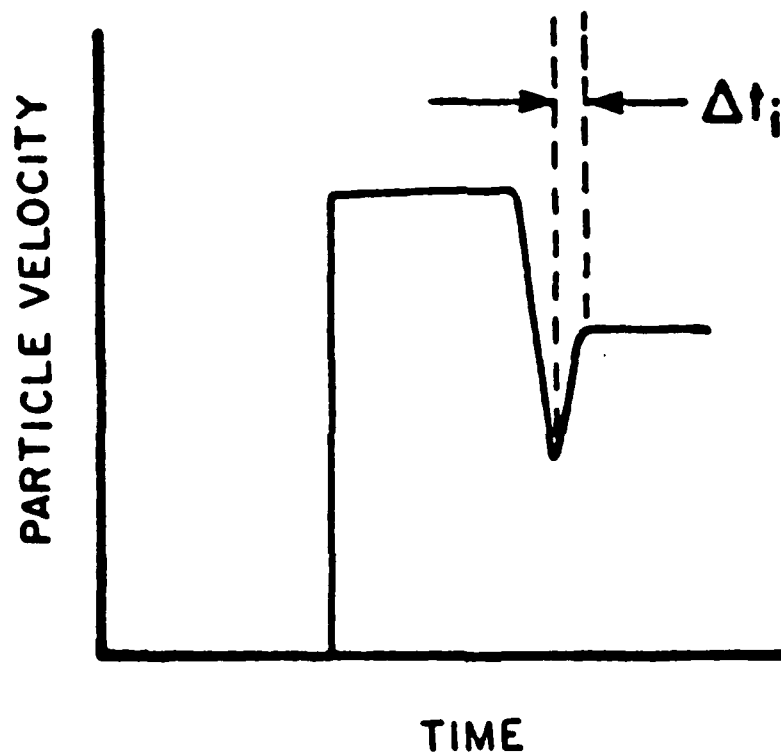


FIGURE 14: Hypothetical velocity history showing the abrupt slope change that is associated with spall.

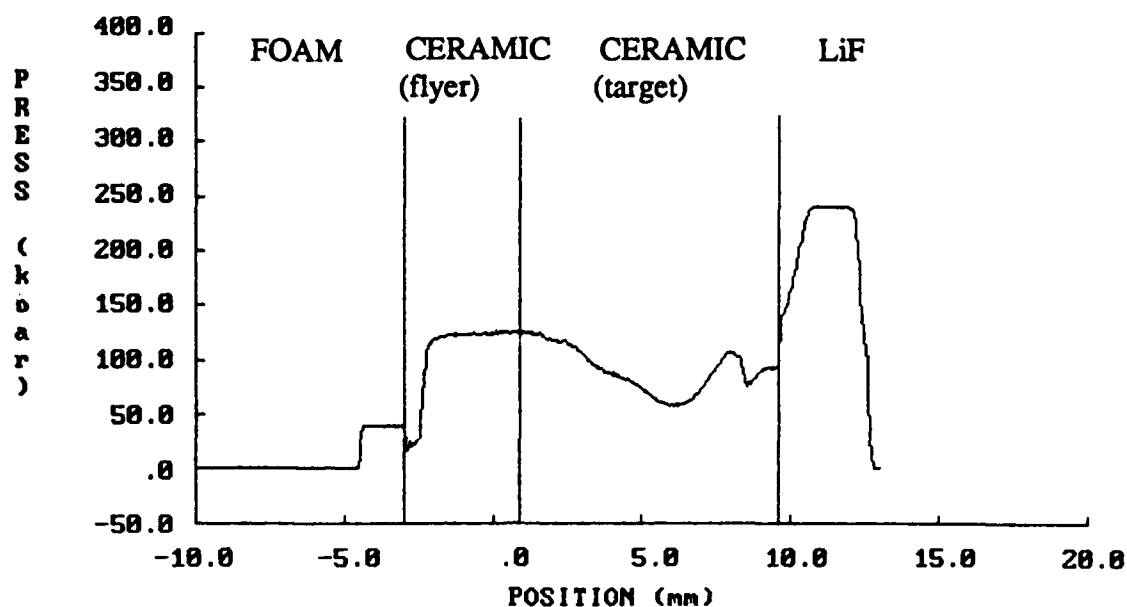


FIGURE 15: Calculated pressure distribution versus position for SiC with a plate impact velocity of 2100 m/s when the pressure reaches its absolute minimum in the target plate.

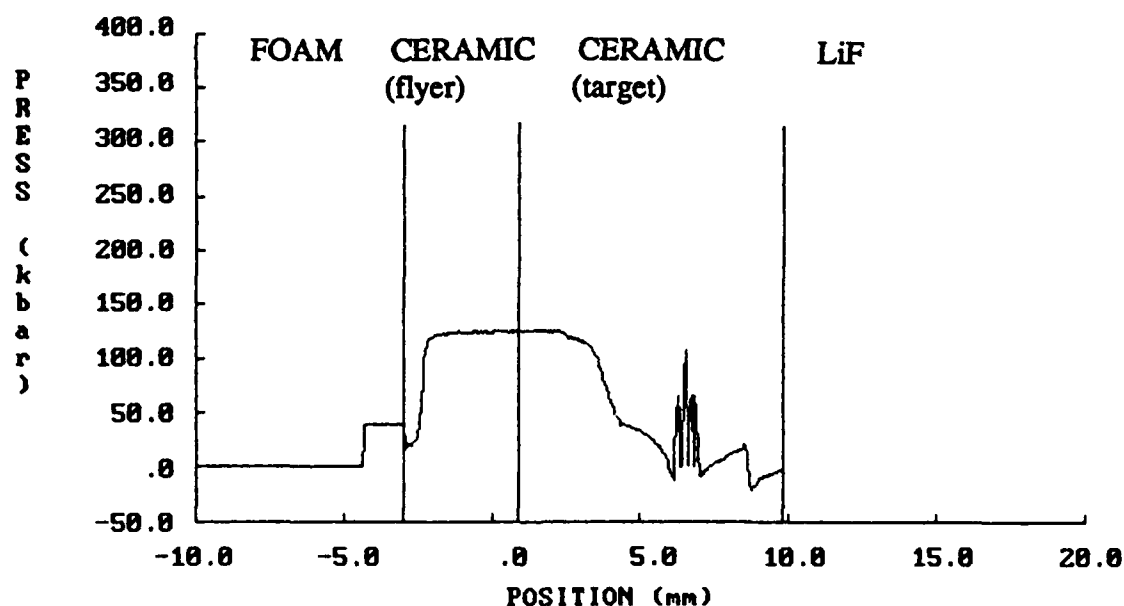
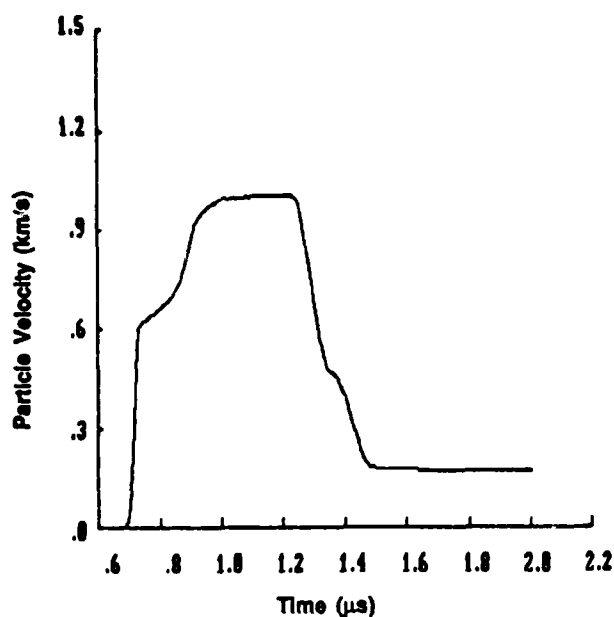
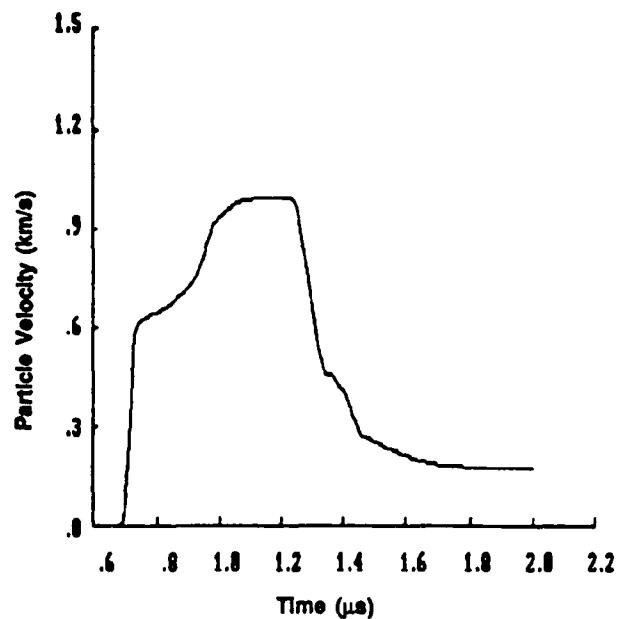


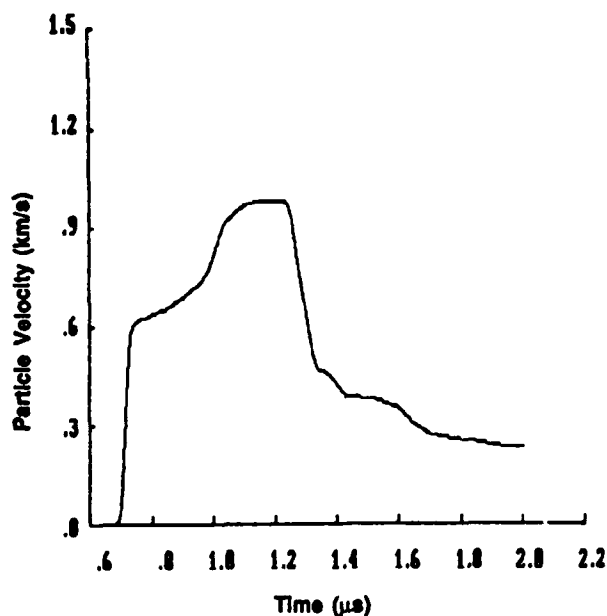
FIGURE 16: Calculated pressure distribution for SiC with a plate impact velocity of 2100 m/s when the lithium fluoride window has been removed. Note the signature of a spall zone at a position 6 to 7 mm from the flyer/target plate interface.



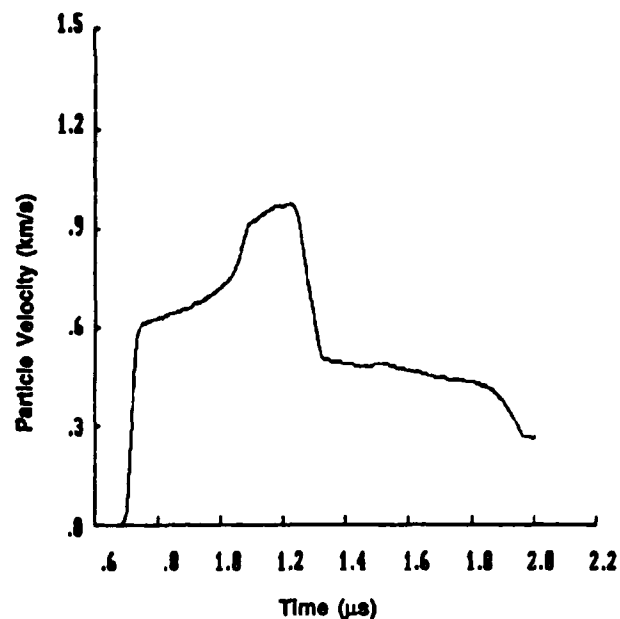
(a) $\alpha = 0.6 \times 10^{-6}$



(b) $\alpha = 2 \times 10^{-6}$



(c) $\alpha = 3 \times 10^{-6}$



(d) $\alpha = 4 \times 10^{-6}$

FIGURE 17: Model predictions with an increase in the damage coefficient α using the parameters; $C_1 = 80$, $C_2 = 100$, $n = 0.1$, and $C_3 = 0.008$ for SiC with plate impact velocity of 2100 m/s reduces the elastic unload and shows a more dispersive plastic unload wave.

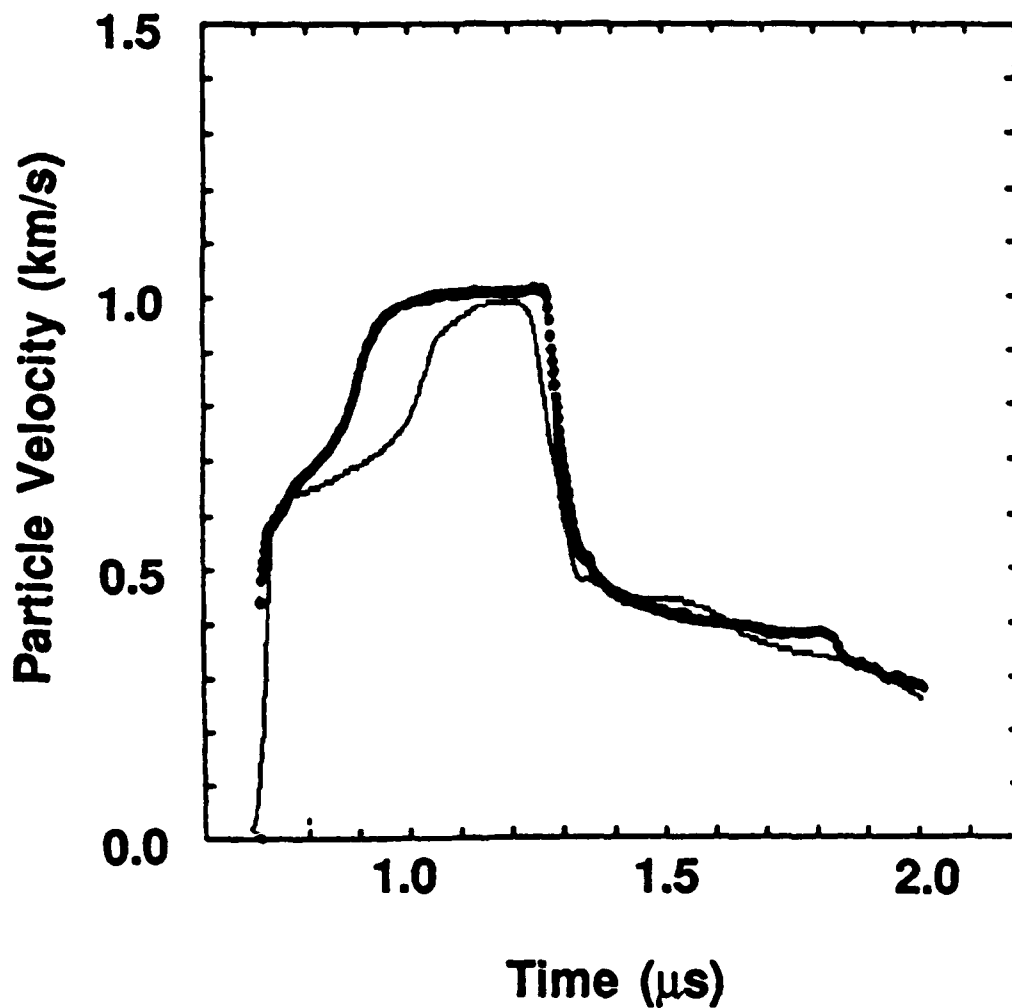


FIGURE 18: Comparison of PC-WONDY model predictions with experimental data for SiC with plate impact velocity of 1540 m/s and with increased damage accumulation. The damage was increased from 6 - 8 percent (see figure 15) to 40 percent. This produces good agreement to the experimental data shown with the heavy line (Kipp and Grady, 1989), for times greater than 1.3 μ s after plate impact. Suggestion is that after the loading phase, damage continues to accumulate, reaching a level of about 40 percent by the time unloading begins.

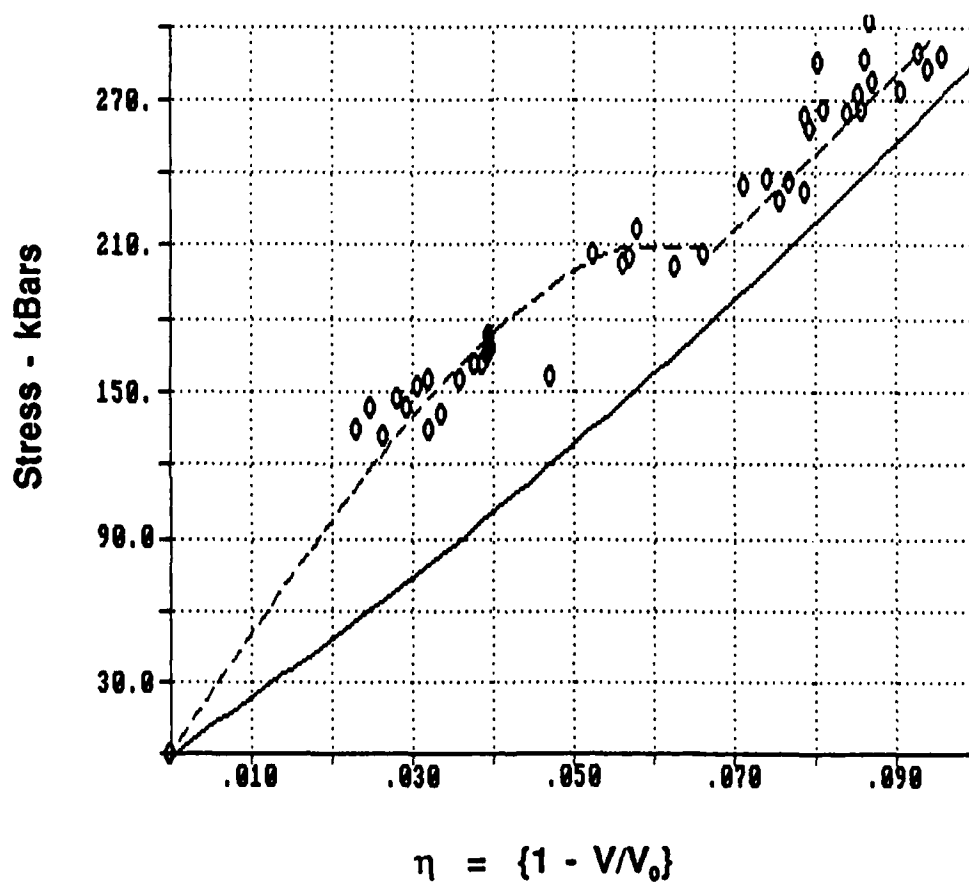


FIGURE 19: Least squares fit of Hugoniot data for B_4C (Gust et al, 1971) using equation 5 for values of η greater than 0.15 (solid line). The observed $\Delta\eta$ at constant stress for $\eta = .055$ to .065 is indicative of possible loss of porosity or phase change in the ceramic. The shape of the underlying hydrostat is therefore not known.

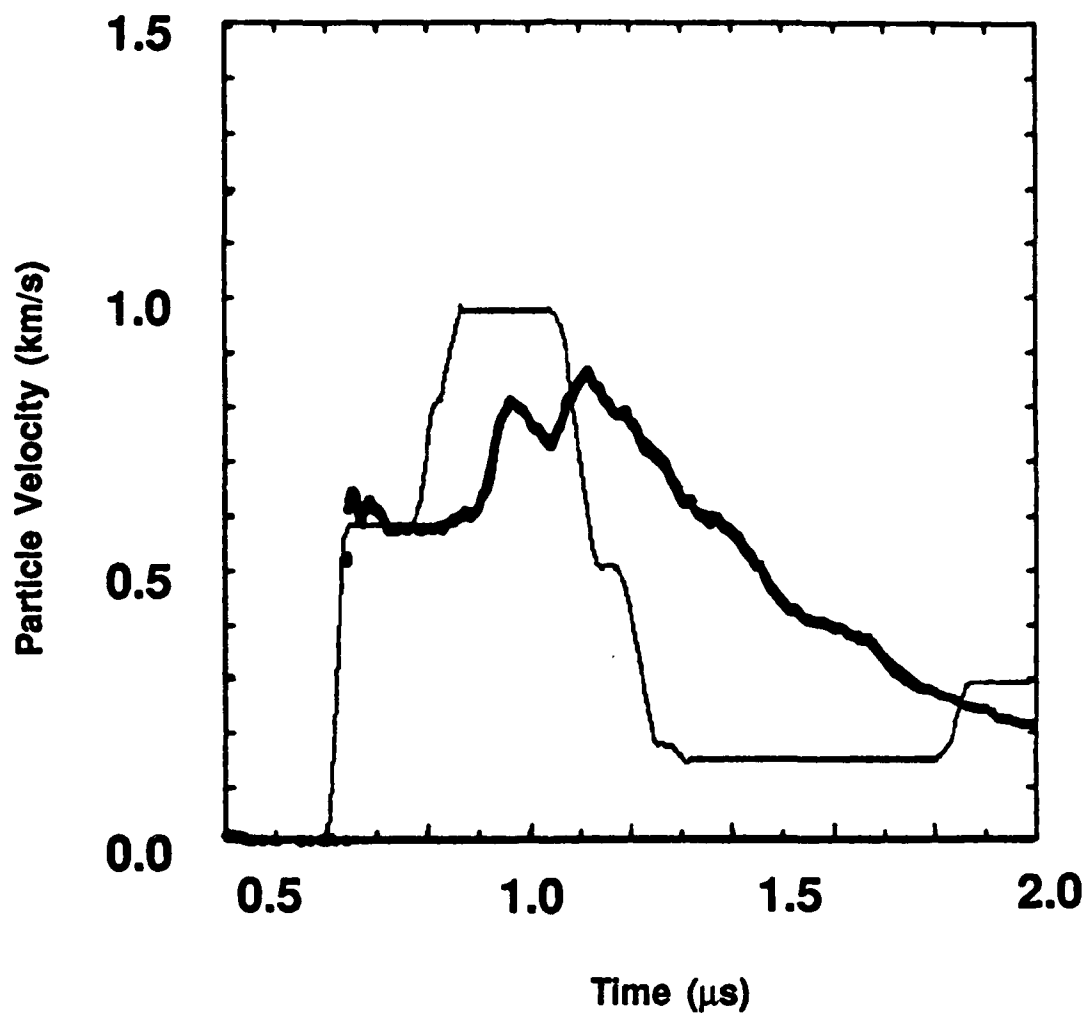
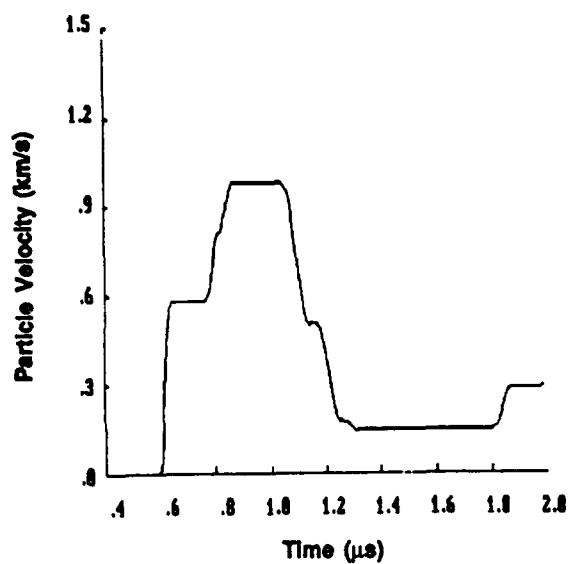
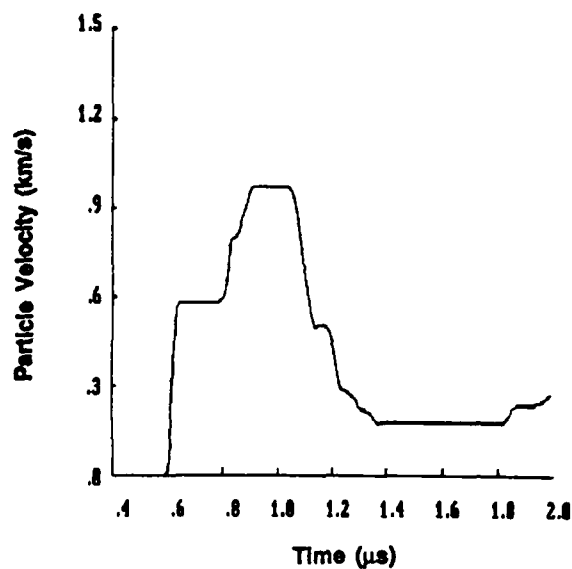


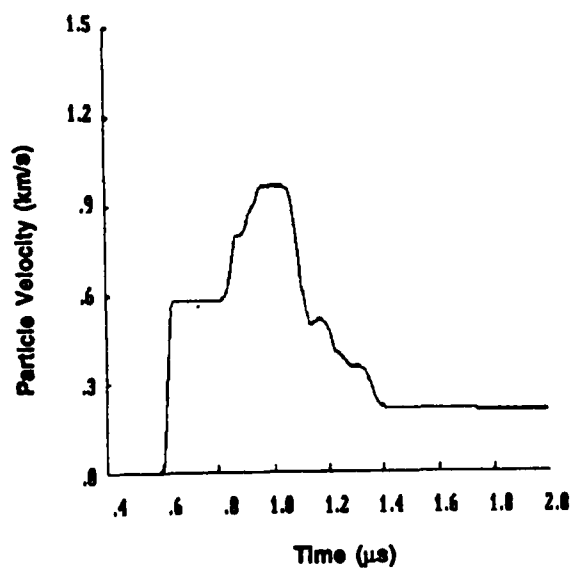
FIGURE 20: Comparison of PC-WONDY model predictions with experimental data for B_4C using an elastic perfectly-plastic model for plate impact velocity of 1550 m/s. Experimental results shown with the heavy line (Kipp and Grady, 1989).



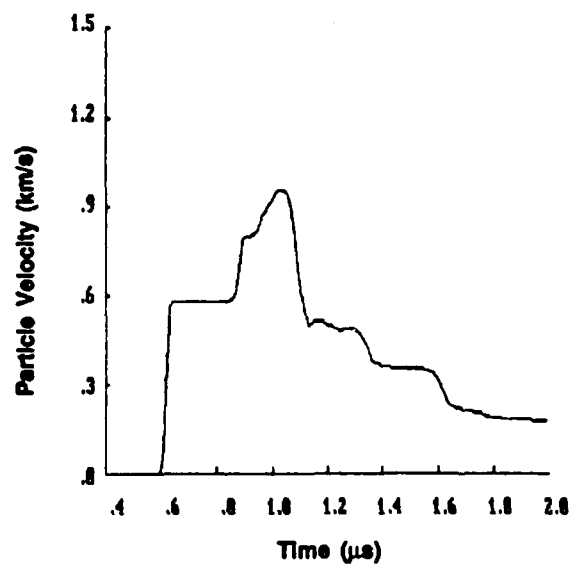
(a) Perfectly-plastic



(b) $\alpha = 1.0 \times 10^{-5}$



(c) $\alpha = 2.0 \times 10^{-5}$



(d) $\alpha = 3.0 \times 10^{-5}$

FIGURE 21: Model predictions of velocity history curves for B_4C for plate impact velocity of 1550 m/s with variation in the damage sensitivity. Increases in α delays the arrival time of the plastic shock. The elastic unloading wave begins to catch up to the plastic load, overtaking it in (d).

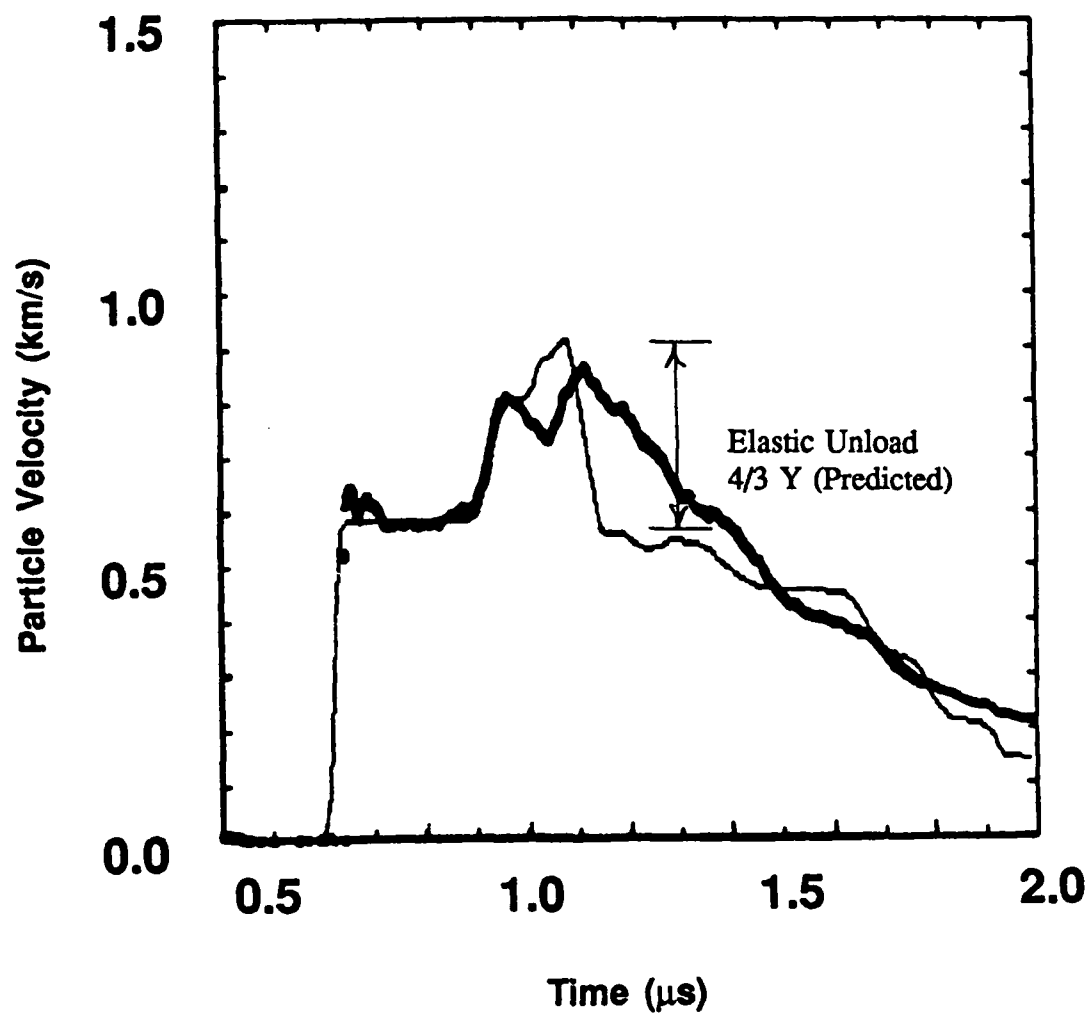


FIGURE 22: Comparison between model predictions and measured velocity histories for B_4C , using $\alpha = 3.4 \times (10)^{-5}$ kg/J, $C_1 = 116$, and no work hardening or strain rate hardening adequately fits the loading waves for plate impact velocity of 1550 m/s. Heavier curve is experimental data (Kipp and Grady, 1989).

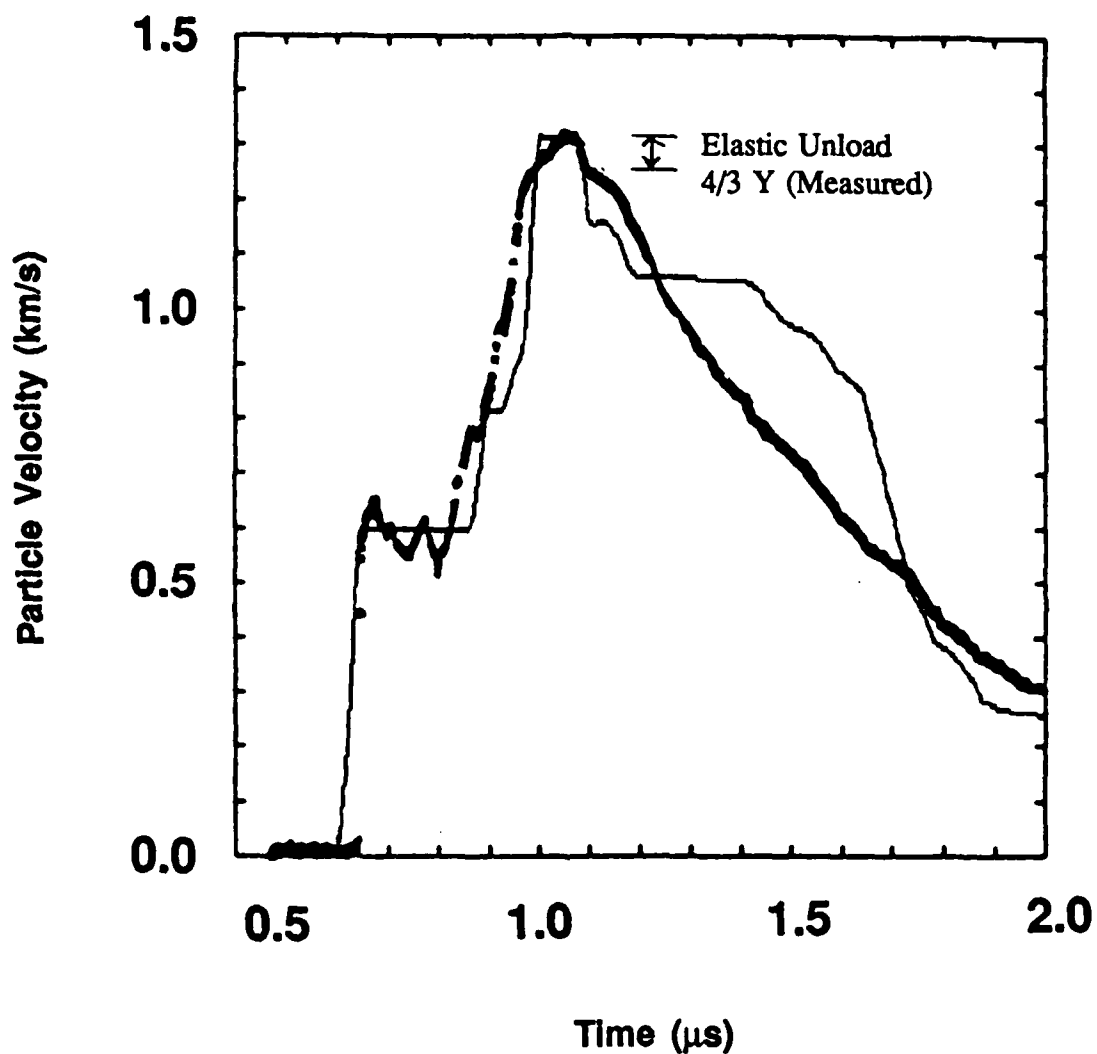


FIGURE 23: Comparison between model predictions and measured velocity histories for B_4C , using $\alpha = 3.4 \times 10^{-5}$ kg/J, $C_1 = 116$, and no work hardening or strain rate hardening adequately fits the loading waves for plate impact velocity of 2210 m/s. Heavier curve is experimental data (Kipp and Grady, 1989).

APPENDIX 1

RDA CERAMIC FAILURE MODEL

TENSILE DAMAGE MODEL:

A material is said to be brittle under conditions in which its ability to resist loads decreases with increasing deformation [1]. In order to solve high velocity impact problems with a hydro code the total stress is decomposed into hydrostatic and deviatoric components. To characterize the brittle nature of ceramics it is necessary to modify the usual linear elastic relationships for stress and strain. The expressions for deviatoric and volumetric stress are therefore written in the following form,

$$P = 3K (1 - D) \phi \quad (1-1)$$

$$S_{ij} = 2G (1 - D) e_{ij} \quad (1-2)$$

where P is the pressure, S_{ij} and e_{ij} are the deviatoric components of stress and strain, respectively, ϕ is the volumetric strain, K and G are the undamaged bulk and shear moduli of the material, and D is a state variable describing the internal damage in the material.

The underlying concept of this model is that of a degraded bulk modulus \bar{K} , and a degraded Poisson's ratio $\bar{\nu}$, (Budiansky and O'Connell [6]), where

$$\bar{K} = K (1 - 16/9 f(\bar{\nu}) C_d) \quad (1-3)$$

$$\bar{f}(\bar{\nu}) = (1 - \bar{\nu}^2) / (1 - 2\bar{\nu}) \quad (1-4)$$

$$\bar{\nu} = \nu (1 - 16/9 C_d) \quad (1-5)$$

Here ν is the undamaged Poisson's ratio and C_d is the crack density, or void volume of the material.

Grady and Kipp [3] proposed that the number of flaws per unit volume at a given pressure could be described statistically using a Weibull distribution

$$N = k (P/3K)^m \quad (1-6)$$

An expression for fragment diameter as a function of strain rate was also derived by Grady [4]

$$d = \left(\frac{\sqrt{20} K_{1c}}{\rho C \dot{\phi}} \right)^{2/3} \quad (1-7)$$

Taylor et al [5] replaced the quantity ϕ with ϕ_{\max} , the maximum strain at failure. They also postulated that the characteristic flaw size was proportional to the radius of the fragment size, i.e., $a \sim 1/2d$. Then, defining the average volume of each flaw as βa^3 , where β is an unknown proportionality constant, an expression for crack density, independent of Budiansky and O'Connell was given as

$$C_d = N \beta a^3 \quad (1-8)$$

or expanding,

$$C_d \frac{5}{2} \frac{k}{(3K)^m} = \left(\frac{K_{1c}}{\rho C} \right)^2 P^m \dot{\phi}_{\max}^{-2} \quad (1-9)$$

where,

P = tensile pressure

k, m = Weibull parameters

K_{1c} = fracture toughness

ρ = density

C = sound speed

$\dot{\phi}_{\max}$ = maximum strain rate at failure

Inspection of (1-3) indicates that a convenient expression for damage is

$$D = 16/9 f(\bar{v}) C_d \quad (1-10)$$

Arbitrarily setting a limiting value of crack density, C_d , to 9/16, it follows that the damage varies smoothly from 0 to 1 as the void fraction varies from 0 to 9/16, or to slightly more than one-half its total volume.

In order to describe the state of the material, for a given set of volumetric and deviatoric strain rates, the quantities C_d , D , P , and S_{ij} must be solved for. These are time integrated quantities and therefore must be put into rate form. Taking the time derivatives of (1-9), (1-10), (1-1), and (1-2), holding the strain rates constant, the final form of the rate expressions given by Taylor et al is,

$$\dot{C}_d = \frac{5}{2} \frac{km}{(3K)^{m-1}} \left(\frac{K_{1c}}{\rho C} \right)^2 p^{m-1} \dot{\phi} \dot{\phi}_{\max}^{-2} \quad (1-11)$$

$$\dot{D} = \frac{16}{9} \left[f_1(\bar{v}) \dot{C}_d + \dot{C}_d f_1(\bar{v}) \right] \quad (1-12)$$

$$\dot{P} = 3K[(1 - D) \dot{\phi} - \dot{\phi} D] \quad (1-13)$$

$$\dot{S}_{ij} = 2G[(1 - D) \dot{e}_{ij} - \dot{e}_{ij} D] \quad (1-14)$$

We immediately make a substitution in 1-11, replacing $\dot{\phi}_{\max}$ with $\dot{\phi}$ as was in the original formulation of Grady and Kipp. Second, in order for these rate equations to be well behaved as the material cycles from tension to compression and back an important modification must be made. Both the strain terms, ϕ and e_{ij} , in equations 1-13, and 1-14 must be regarded as the integrated strains for a given tensile cycle, that is, strains that resulted in the presence of damage accumulation. Once the material unloads or goes into compression other stress rate expressions¹ are used leading to solutions in stress and strain space inconsistent with what would result from equations 1-13 and 1-14 had they been used. Referring to Figure 1-1a and 1-1b we note that residual strains can exist due to plasticity in both tension and compression. For example a condition of zero stress can exist with finite strain. We can see by inspection of 1-13 and 1-14 that the presence of this residual strain coupled with a high damage rate can

¹The material is assumed to unload in tension, and load and unload in compression linear elastically. Plastic flow in compression is governed by the von Mises incremental theory of plasticity.

produce a significant negative stress rate even though the imposed strain rate is positive. It is this inconsistency that leads to accumulation of negative energy i.e. products of negative stress rates with positive strain rates and must be corrected.

Fortunately the process of correcting this situation is simple and straight forward. Any time the material enters a new tensile cycle the residual strain is 'trapped'. All subsequent strains for this tensile cycle are corrected by this amount. The strains used in the rate equations are

$$\phi_l = \phi_g - \phi_r \quad (1-17)$$

where

ϕ_l = local strain

ϕ_g = global (solution strain)

ϕ_r = residual ('trapped') strain

The stress rate equations now become

$$\dot{P} = 3K[(1 - D) \dot{\phi}_v - \dot{\phi}_v^* D] \quad (1-18)$$

$$\dot{S}_{ij} = 2G[(1 - D) \dot{e}_{ij} - \dot{e}_{ij}^* D] \quad (1-19)$$

where star '**' denotes the corrected, or local strains. Now, when the material goes through a compression - tension transition, stress time histories are smooth and well behaved.

Numerical stability is regained.

COMPRESSIVE DAMAGE MODEL:

The compressive damage model is a plasticity based engineering model. Damage is included as a softening term in Johnson and Cook's expression for the yield surface of a ductile material [7],

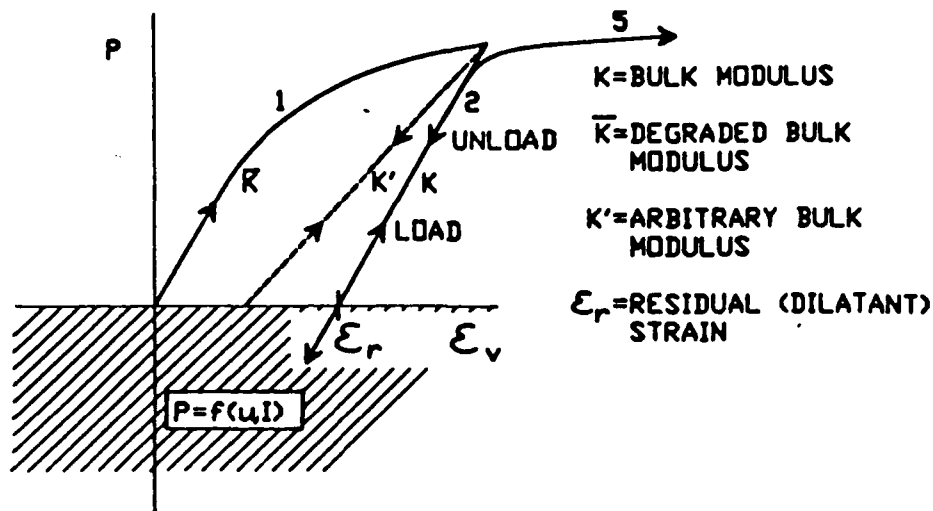
$$Y = ((C_1 + C_2 \epsilon_p^n) (1 + C_3 \ln \epsilon^*) (1 - T^{*m}) + C_4 P) (1 - D) \quad (1-20)$$

where C_1 is the static yield strength, C_2 and n are the strain hardening parameters, C_3 is the viscoplastic (strain rate) parameter, T^* and m are the thermal softening terms, c_4 is the confining pressure parameter, and $(1-D)$ is the damage induced softening term.

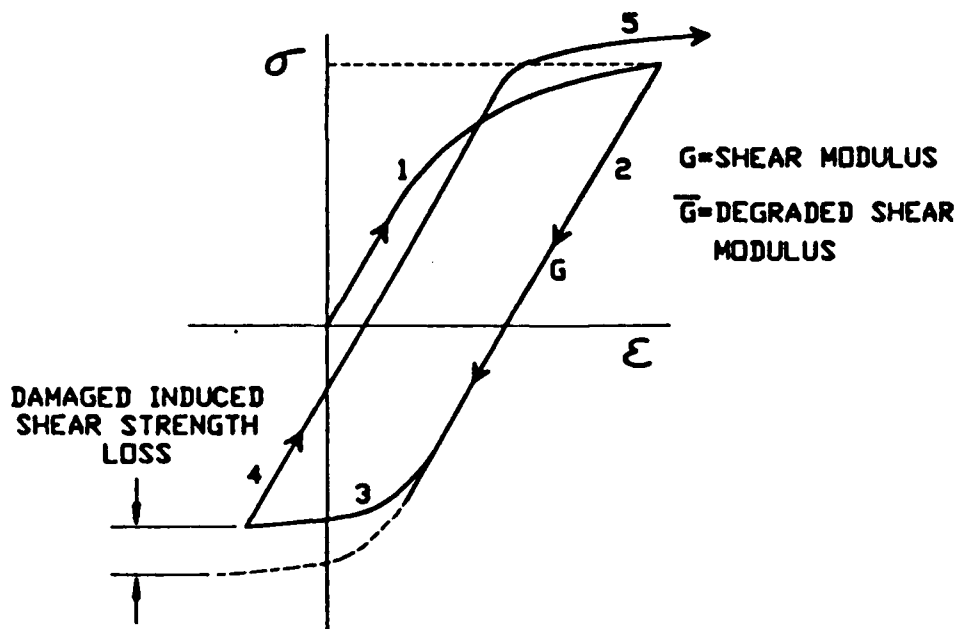
The damage evolution is related to the plastic shear work rate in compression and allows for a single damage sensitivity parameter, α , to characterize a given materials damage dependence on plastic work rate,

$$\dot{D} = \frac{\alpha \dot{W}_p}{(1 - D)} \quad (1-21)$$

Here D is the same scalar damage state variable as was used in tension. Hence the integrated value for damage during a compressive cycle becomes the initial value for damage in a subsequent tensile cycle and vice versa. Note that any damage evolved in tension will affect the shear strength of the material in compression (eq. 1-20) and that damage evolved in compression will affect the stiffness in tension (eq. 1-1, 1-2). In either case, when the damage reaches one the material loses all ability to support either a tensile bulk or shear load, or a compressive shear load. Program logic however, still allows the material to sustain pure hydrostatic compressive loads.



1-1a. Typical load cycle for hydrostatic component of stress for ceramic model. Damage evolution is reflected in modulus change. Unload path is arbitrary and is used to ascribe dilatancy.



1-1b. Typical load cycle for deviatoric component of stress for ceramic model. Damage accumulation affects both shear modulus in tension and yield surface in compression.

APPENDIX 2

FORMULARY

Bulk sound speed:

$$C_o^2 = C_L^2 - 4/3 C_s^2 \quad (2-1)$$

Poisson's ratio:

$$\nu = \frac{C_L^2 - 2C_s^2}{2(C_L^2 - C_s^2)} \quad (2-2)$$

Isentropic (cold compression) pressure:

$$P = \rho_o u_s u_p \quad (2-3)$$

$$\eta = \frac{u_p}{u_s} \quad (2-4)$$

Assuming

$$u_s = C_o + s u_p \quad (2-5)$$

then

$$P = \frac{\rho C_o^2 \eta}{(1-s\eta)^2} \quad (2-6)$$

Shock impedance:

$$Z_L = \rho_o C_L \quad (\text{for ceramic with strength}) \quad (2-7)$$

$$C_L = \frac{\sqrt{3(1-\nu)}}{(1+\nu)} u_s \quad (2-8)$$

$$Z_L = \rho_o u_s \quad (\text{for LiF with no strength}) \quad (2-9)$$